Strong coke-resistivity of spherical hollow Ni/SiO₂ catalysts with shell-confined high-content Ni nanoparticles for methane dry reforming with CO₂

Mohammadreza Kosari [a,b], Saeed Askari [a], Abdul Majeed Seayad [b], Shibo Xi [b], Sibudjing Kawi [a], Armando Borgna [b,*], Hua Chun Zeng [a,*]

[a] Department of Chemical and Biomolecular Engineering, Faculty of Engineering, National University of Singapore, 10 Kent Ridge Crescent, 119260, Singapore
[b] Institute of Sustainability for Chemicals, Energy and Environment (ISCE²), Agency for Science, Technology and Research in Singapore (A*STAR), 1 Pesek Road, Jurong Island, 627833, Singapore

ARTICLE INFO

ABSTRACT

Hollow nanocatalysts, which are vehemently researched for their delimited cavity and enclosed shell, could manifest tunable focal properties besides well-defined active sites, thus enhancing the catalytic functionality. Herein, nickel-silicate hollow spheres (NHSs) with varied shell thickness and interior cavity size were commensurately designed. Distinction between various NHSs-derived Ni/SiO₂ with identically mimicked morphologies was realized by examining their catalytic performance for methane dry reforming (DRM) reaction with sweeping pre- and post-reaction characterizations (TEM, XPS, XANES, in-situ DRIFTS). Besides facilitating the DRM reaction up to its thermodynamic limit, it was revealed that optimal NHS conformation is beneficial as a potential natural barrier against sintering and coking bottlenecks. Furthermore, a fine-tuned shell composition could endow improved Ni-sintering resistivity and enhanced reactivity to the NHS nanocatalysts. Our findings prove that the hollow interior space with a conducive shell thickness positively influences the reactant conversion and coking hindrance during the DRM reaction.

1. Introduction

The features of hollow nanomaterials (i.e., hollow interior, shell structure, shell thickness, shell curvature, and shell composition) are known to play important roles that significantly affect the functionality and performance [1]. In the field of heterogeneous catalysis, for example, sphere radius variation of copper-silicate hollow spheres, a subsidiary of transition metal-silicate hollow spheres derived from Stöber silica beads [2], was found to balance the trade-off amongst surface conformation, reactants diffusion flux and adsorption, and ultimately, catalytic performance [3]. Shell thickness [4], hollowness [5], number of shells [6], and shell composition [7] are also believed to be as imperative as surface conformation (e.g., concave and convex curvature conformations [8]) on the reaction rate that need in-depth investigation. However, quest for finding effective protocols to tune morphological structures (e.g., shell thickness) of such hollow systems is underway to overcome limitation of such morphology-functionality studies. Perhaps, one study that haphazardly examined the hollowness controllability

during a one-pot hydrothermal procedure for synthesizing metal-silicates hollow spheres was a report by Yec et al. in 2014 [9]. The role of different metal salts was explored and demonstrated to have significant effect on the morphology of resultant manganese-silicate hollow spheres. Although this study provided a unique protocol for the controlled synthesis of manganese-silicate hollow spheres, neither the shell thickness and hollow core size variability nor the morphology-functionality relationship on the catalytic performance was evaluated. Except for metal-silicate hollow spheres, recent endeavors on gaining control over the shell-thickness and shell-robustness of hollow materials promise greater opportunity to experimentally increase the understanding of morphology-functionality relationship of hollow architectures. Wang et al. developed an effective protocol to precisely control shell thickness of mSiO₂-based nanocapsules with cavity-confined, fine Ni NPs with the shell size range of 2.9–8.1 nm which allowed further elucidation on the role of shell diffusion effect versus shell thickness [10]. Other conceptually analogous works reported by Seo et al.,[11] Zhang et al.,[12] Zeng et al.,[13] Yang et al.,

---

[14] Li et al.,[15] and Xu et al.[16] also provide insightful inferences on the intrinsic effect of focal features (e.g., shell-thickness) of core-shell and yolk-shell structures on the performance and kinetics of a typical reaction.

Herein, we fabricated a series of nickel-silicate hollow spheres (NiSiO HS or NHS) with different shell thicknesses (or hollowness), while retaining other structural properties and the nature of active sites to be identical. Though many methods of preparing nickel-silicate hollow spheres have been reported, fine-tuning of their morphology is still limited. Hu et al. reported one of the earliest nickel-silicate hollow spheres utilizing a PMMA-CS$_2$-ethanol-aqueous system (PMMA: polymethyl methacrylate) [17]. Jin et al. prepared nickel-silicate hollow spheres from Stöber silica via a solvothermal method followed by an etching process [5]. Hydrothermal-based sacrificial dual-templating and hard-templating methods were also developed for the preparation of uniform nickel-silicate hollow spheres and other transition metal-silicates from Stöber silica beads [9,18]. Apart from these progresses, practical studies on engineering morphological structure of nickel-silicate hollow spheres or other metal-silicate hollow spheres in general are still lacking.

Application wise, limited reports exist regarding the hollow features (especially shell thickness) on metal nanoparticle sintering or reaction performance of the hollow sphere supporting metal catalysts. For example, as reported recently [19], a sandwiched mSiO$_2$@Ni@mSiO$_2$ with Ni NPs clamped between two layers of mesoporous silica led to an average 50% CH$_4$ conversion for unpromoted mSiO$_2$@NiSiO@mSiO$_2$, while an improved CH$_4$ conversion of about 65% was observed for the promoted mSiO$_2$@NiCoSiO@mSiO$_2$ in dry reforming of methane (DRM). The proposed sandwich-like structure consists of an externally coated silica layer on top of a nickel-silicate layer that assist to inhibit sintering of derived Ni NPs by clamping them between the silica layers (i.e., anchoring Ni NPs fully stationary). However, a closer look at this morphology indeed reveals that a very limited reaction space is lent to Ni sites (insufficient inner cavity surrounding the entrapped Ni NPs) which was reported to be quite undesirable for DRM reaction. According to Wang et al., narrower reaction space surrounding Ni sites could result in carbon accumulation and hence increase Ni aggregation and coking [20]. Therefore, besides developing hollow silica spheres with shell-contained Ni NPs and alterable focal features (shell thickness and hollow core size), it will be appraised whether inner cavity of such hollow spheres with Ni NPs confined in their shell could affect DRM reaction performance such as coking. Such hollow Ni/SiO$_2$ could offer sufficiently maximal inner cavity increasing Ni dispersion and the number of active Ni sites within the shell besides providing a key environment for a consistent yet effective carbon gasification in DRM reaction [20,21].

As illustrated in Scheme 1, herein we propose a synthetic protocol to vary shell thickness and cavity size of nickel-silicate hollow spheres which are categorized into two main groups. First, a template material with different preparation pathways could render distinct hollow morphologies. Accordingly, two starting silica precursors were used in this work: Stöber silica sphere (SiO$_2$) and mesoporous silica sphere (MSS). Second, depending on the precursor, the process requires a different approach. For SiO$_2$, it is shown that its architectural alteration by adding another coating layer of silica could lead to controlling the shell thickness of the final nickel-silicate hollow spheres. For MSS, however, the effect of different hydroxide ions stemmed from different bases is found to have imperative effect on both the shell thickness and interior cavity size. Along the same line, a ratio of two bases has also been found to pose a "swelling" effect on hollow spheres, resulting in their thickness and cavity size changing. To appraise the role of shell thickness, interior cavity size, and topology of nickel-silicate hollow spheres, we targeted catalytic biogas dry reforming to distinguish the catalytic performance for such compositionally alike but morphologically different hollow nickel-based materials.
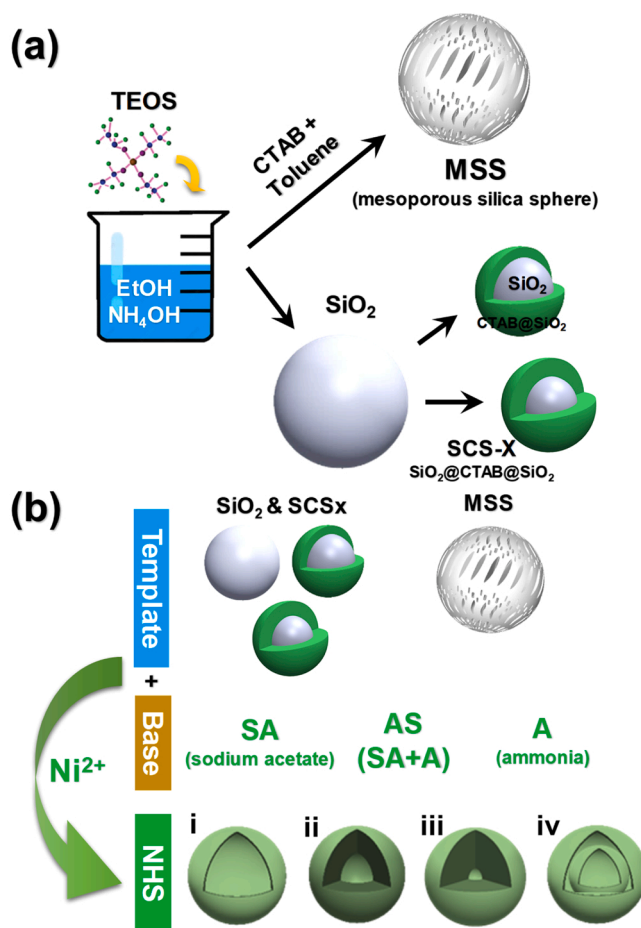
Scheme 1. Schematic illustration of synthetic processes of nickel-silicate hollow spheres (NHS) demonstrating varied shell thickness and interior cavity size hollow spheres by template and base alteration. (a) Preparation of different silica templates (i.e., SiO$_2$ spheres, SiO$_2$ coated with another CTAB-SiO$_2$ shell (SCSx, where x represents the amount of TEOS used), and mesoporous silica spheres (MSS)). (b) Alteration of reaction base source (i.e., sodium acetate (SA), ammonia (A, NH$_4$OH), and their combination (AS)) depending on the silica template used, which are as follows: (i): thin-shell NHS (by utilizing SiO$_2$ or MSS with SA base), (ii and iii): thick-shell NHS (by utilizing SCSx with SA base and/or MSS with NH$_4$OH or MSS with a ratio of SA/NH$_4$OH), (iv): double-shell NHS (by utilizing SCS-0.6 with SA base).

2. Experimental section

2.1. Chemicals

The following chemicals were used as received without any further purification: tetraethyl orthosilicate (TEOS, 99%, Aldrich), cetyltrimethylammonium bromide (CTAB, 96%, Aldrich), nickel (II) sulfate (Ni(SO$_4$)$_2$, > 98.0%, Aldrich), cerium (II) nitrate (Ce(NO$_3$)$_2$, > 98.0%, Aldrich), sodium acetate anhydrous (99%, Fisher), ammonium hydroxide solution (NH$_4$OH, 25% NH$_3$ in water, Merck), toluene (>99.5%, VWR Chemicals), absolute ethanol (EtOH, analytical reagent-grade, VWR), and deionized water (DIW, Elga Micromeg Purified Water).

2.2. Synthesis of silica/silicate precursors

2.2.1. Stöber silica beads (Stöber SiO$_2$)

To prepare monodispersed SiO$_2$ beads, modified Stöber method was employed. Under vigorous stirring, TEOS (2.5 mL) was introduced to absolute ethanol (46 mL) followed by immediate addition of NH$_4$OH (5 mL). After 4 h of constant stirring, the milky solution obtained was

centrifuged and the precipitate was washed by EtOH twice. The resultant sample was air-dried at 80 °C.

2.2.2. Mesoporous silicate spheres (MSS)

The MSS powder is produced by mixing an aqueous solution with an organic solution followed by an aging process under no agitation [22]. First, the organic solution was prepared by mixing CTAB (150 mg), EtOH (24 mL), TEOS (180 μL), and toluene (0.6 mL). Simultaneously, the aqueous solution was made by mixing DIW (24 mL) and NH_4OH (0.75 mL). After 10 min of mixing the two solutions, the aqueous solution was rapidly added to the organic solution. Immediately after that, the mixing was stopped and the mixture was aged at room temperature for 4 h. Finally, white MSS product was centrifuged, washed by EtOH twice, and air-dried at 80 °C.

2.2.3. SiO_2@CTAB-SiO_2 (SCS) with different coating thickness

To coat another layer of mesoporous silica on the outer surface of Stöber SiO_2 beads, a surfactant method was used. Firstly, Stöber SiO_2 (100 mg) was dispersed in DIW (20 mL) by sonication for 30 min. Meanwhile, a separate beaker was charged with CTAB (150 mg), EtOH (30 mL), DIW (30 mL), and NH_4OH (0.55 mL). After stirring for 10 min, the Stöber SiO_2 suspension was gently added to the beaker followed by dropwise addition of the required amounts (0.1, 0.3, and 0.6 mL) of TEOS. After stirring for 4 h, the product was separated by centrifugation and washed twice with EtOH followed by air-drying at 80 °C. The product was denoted as SCSx, where x stands for the amount of TEOS (mL) added in each synthesis. Accordingly, the samples SCS0.1, SCS0.3, and SCS0.6 were prepared.

2.3. Synthesis of nickel-silicate hollow spheres (NHS) and metal doping

An aqueous silica suspension using SiO_2 or SCSx, or MSS of concentration of 30 mg·mL^{-1} was initially prepared by sonication. To a 50 mL Teflon-lined autoclave reactor, DIW (30 mL), aqueous nickel sulfate solution (0.02 M, 2.5 mL), aqueous sodium acetate solution (0.5 M, 2 mL), and the silica suspension were added. After closing the stainless-steel autoclave, the reaction was carried out to 160 °C for 10 h. The reactor was then cooled down to room temperature and the final product was centrifuged, washed twice with EtOH, and finally air-dried at 80 °C. For SiO_2 and SCSx precursors, aqueous solution of sodium acetate was used. In addition to the use of sodium acetate, pure NH_4OH solution (25 wt%, 3 mL) and mixture of NH_4OH/sodium acetate (according to the stated recipe in Table 1) were also used during the above hydrothermal conversion of MSS precursor.

To expose a second metal component as a dopant, such as cerium, onto the metal-silicate interfaces, the same one-pot hydrothermal treatment method could be utilized [18]. Therefore, a dopant metal can be supplanted into the NHS-SiO_2-S structure during its hydrothermal synthesis stage either by replacing or adding certain amount of metal salt solution. In this case, for synthesizing cerium-doped NHS-SiO_2-S for instance, 1 mL of 0.02 M $Ce(NO_3)_2$ solution in addition to 2 mL 0.02 M $Ni(SO_4)_2$ solution was used.

2.4. H_2-reduced nickel-silicate hollow spheres

Nickel-silicate hollow spheres (NHS) were reduced in a tube furnace with the following experimental conditions: H_2 flow = 50 mL·min^{-1}, ramp rate = 3 °C min^{-1}, T = 700 °C, time = 4 h. After the reduction, the resultant black powder was obtained and stored under nitrogen.

2.5. Materials characterization

Transmission electron microscopy was employed to unveil sample morphology and interior structure (TEM, JEOL JEM- 2010, 200 kV). In addition, energy-dispersive X-ray spectroscopy (EDX, Oxford Instruments, model 7426) coupled to high-resolution TEM (HRTEM, JEOL JEM-2100 F, 200 kV) was utilized to reveal elemental composition. Nitrogen physisorption analyzer was used to measure specific surface area and pore size distribution after an overnight degassing under constant N_2 flow at 150 °C (Quanta-chrome Instruments NOVA 4200e operating at 77.3 K). Fourier transform infrared spectroscopy in the range of 4000–400 cm^{-1} was used to identify structural and bonding information of nickel-silicate hollow spheres (FTIR, Bio-Rad FTS-3500ARX). Powder X-ray diffraction was also employed to unravel phasic structure and crystallographic information (XRD, Bruker D8 Advance system, Cu K$_\alpha$ radiation at 1.5406 Å). Inductively Coupled plasma optical emission spectrometer (ICP-OES) was used to quantify nickel assay by dissolving 20 mg sample in a concentrated solution of nitric acid (HNO_3) and hydrofluoric acid (HF) with 1:1 v/v ratio and diluting with DIW before analysis. Hydrogen temperature reduction analysis was used to analyze hydrogen consumption and evaluate reduction temperature of nickel-silicate samples (H_2-TPR, TPDRO 1100 system, Thermo Scientific, equipped with a thermal conductivity detector (TCD)). After having degassed at 50 °C for 0.5 h under argon, loaded sample (20 mg) inside the TPDRO quartz column was heated up from 25° to 950°C with a ramp rate of 10 °C·min^{-1} under a diluted hydrogen flow (50 mL·min^{-1}, 5% H_2/95% Ar). To reveal surface chemical composition, X-ray photoelectron spectroscopy (XPS) was employed by referencing all binding energies (BEs) to C 1 s peak at 284.8 eV arising from C–C bonds (XPS, AXIS-HSi, Kratos Analytical). The XPS was equipped with monochromatised Al K$_\alpha$ X-ray source ($h\nu$ = 1286.71 eV, 5 mA, 15 kV) and a constant analyzer-pass-energy of 40.0 eV, operating at 5×10^{-9} Torr. Thermo-gravimetric analysis (TGA) was performed to measure the deposited carbon amount on Ni/SiO_2 catalysts derived from nickel-silicate after DRM reaction (TGA, Shimadzu DTG-60 thermogravimetric analyzer). Monitoring the weight versus temperature, the spent catalyst was placed in a small alumina crucible cup and heated up to 950 °C with a ramp rate of 10 °C·min^{-1} in static air. The X-ray absorption spectroscopy (XAS) experiments were conducted via X-ray absorption fine structure for catalysis (XAFCA) beamline of Singapore Synchrotron Light Source (SSLS) [23]. A Ni standard foil was used for the energy calibration by alignment of the respective absorption edge. The nickel-silicate samples (as-synthesized, calcined, reduced, and spent) were subjected to X-ray absorption near-edge structure (XANES) and extended X-ray absorption fine structure (EXAFS) at room temperature.

2.6. Performance evaluation of NHS catalysts

Atmospheric biogas reforming to syngas (known as dry-reforming of methane) was tested by loading the NHS catalyst sample inside a quartz tube reactor connected to an online gas chromatography (Agilent 7820 A) equipped with a thermal conductivity detector (TCD). Prior to the reaction, the catalyst was reduced in-situ (700 °C, ramp rate of 3 °C·min^{-1}, 40 mL·min^{-1} of H_2 flow, 4 h). The reaction was initiated by flowing biogas (CH_4/CO_2 = 1:1, 20 mL·min^{-1}) at initial temperature of 400 °C. Catalyst activity was finally measured by calculating CO_2 and CH_4 conversion as well as syngas (H_2/CO) ratio.

Table 1
Standardized labeling of various nickel-silicate hollow spheres (NiSiO-HS or NHS) according to the synthetic condition used.

sample ID	synthetic conditions	
	silica source	base/alkaline
NHS-SiO_2-S	SiO_2	sodium acetate (SA)
NHS-SCS0.1-S	SCS0.1	SA
NHS-SCS0.4-S	SCS0.1	SA
NHS-SCS0.6-S	SCS0.6	SA
NHS-MSS-S	MSS	SA
NHS-MSS-A	MSS	NH_4OH
NHS-MSS-AS0.3	MSS	NH_4OH/SA (2:0.3 v/v)

2.7. Mechanistic study with in-situ DRIFTS

In-situ diffuse reflectance infrared Fourier-transform spectroscopy (in situ DRIFTS) was used to study active intermediates arising from nickel-silicate catalyst during DRM reaction (Frontier MIR with a mercury−cadmium−telluride (MCT) detector and ZnSe cell, PerkinElmer). Firstly, the ex-situ reduced catalyst (700 °C, 40 mL·min^{-1} H$_2$ flow, 3 h) was loaded into the DRIFTS cell and again reduced in-situ (600 °C, 15 mL·min^{-1} H$_2$ flow, 30 min). Subsequently, the background was recorded and the reaction gas was then introduced into the cell (CH$_4$/CO$_2$ = 1/1, 10 mL·min^{-1}) followed by collecting the IR spectra (each 32 times with a resolution of 4 cm^{-1}) at different temperatures ranging from 300° to 600°C with an interval of 50 °C. A pulsed-flow DRIFTS study with individual reactants was used to reveal detailed information onto DRM reaction mechanism on Ni/SiO$_2$ derived from nickel-silicate. To do so, the ex-situ reduced catalyst was placed in the cell and again reduced in-situ, followed by flushing with helium gas for 2 h. The background scan was taken at 500 °C under the He flow, followed by introduction of a short pulse of methane (5 mL·min^{-1} for 20 s). The IR spectra were collected every 20 s (repeated 4 times, resolution at 4 cm^{-1}) after the pulse for 5 min. A CO$_2$ pulse of equal volume was then introduced, followed by another methane pulse and IR spectra were collected with time.

3. Results and discussion

3.1. Nickel-silicate hollow spheres (NHS) with defined hollowness and thickness features

Despite the enormous success in fabrication of uniform metal-silicate hollow spheres [2], there are still important features to be further appraised such as performing functionality, porosity and permeability of shell, interior space, overall structural density, and compositional tunability (e.g., synthesis of hybrid organic/inorganic composites) [24, 25]. Amongst them, the interior space and the functional shell are two important parameters that define the identity of hollow materials.

Except few studies that demonstrated how the shell thickness of pure hollow silica spheres are controlled or different interior cavities are created in silica beads [26,27], there is no report on such controllability for the metal-silicate hollow spheres. Along this line, sacrificial hard-template (or self-template) by hydrothermal method, a more often reported method for synthesizing the hollow metal-silicate spheres or other topographies [28,29], is a facile and practical procedure but with insufficient controllability over the extent of interior cavity and shell thickness. The reason could be potentially due to the simple nature of starting material. Herein, we proposed and demonstrated architectural design of initial silica precursor and related selection of reaction
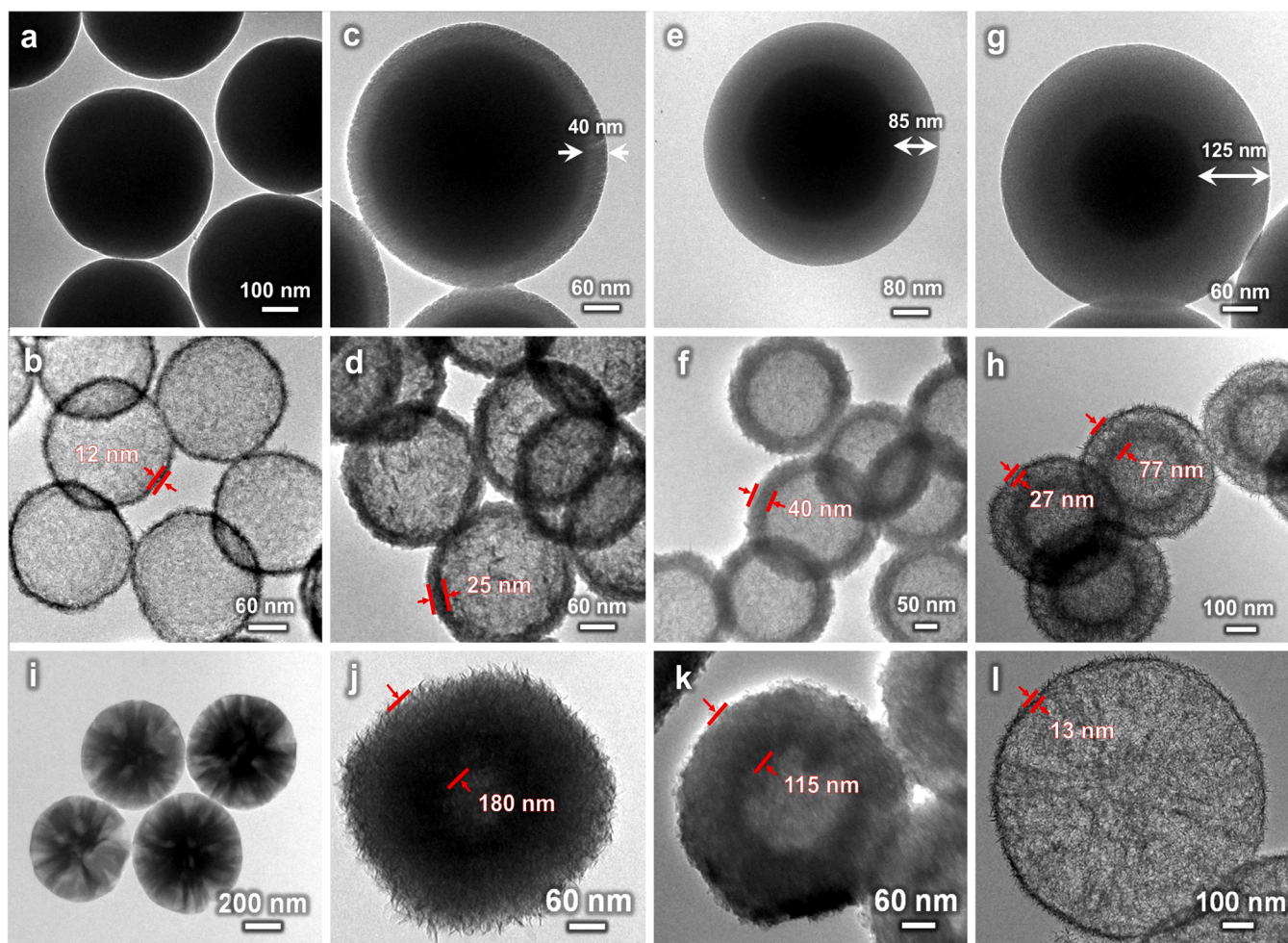

Fig. 1. TEM images of silica precursors (i.e., Stöber SiO$_2$, its derived core-shell SiO$_2$ @CTAB-SiO$_2$ (SCSx), and MSS) as well as their corresponding nickel-silicate hollow spheres (NHS). (a) Stöber SiO$_2$, (c) SCS0.1, (e) SCS0.3, (g) SCS0.6, and (i) MSS. Corresponding NHS derived from each starting material shown in the upper images including (b) NHS-SiO$_2$-S, (d) NHS-SCS0.1-S, (f) NHS-SCS0.3-S, (h) NHS-SCS0.6-S, and (j, k, l) MSS-derived NHS including NHS-MSS-A, NHS-MSS-AS, and NHS-MSS-S. Note that "SCSx" stands for the coated SiO$_2$ spheres with another layer of CTAB-mesoporous silica (SiO$_2$ @CTAB-SiO$_2$) in which "x" is the amount of TEOS (mL) used in the coating process. "S" in the NHS-SiO$_2$-S notation stands for the utilized base "sodium acetate" (Section 2.3). Note that "AS" stands for the hydroxide ratio in which "A" is ammonia and "S" is sodium acetate.

condition for the chosen silica precursor to gain controllability over the final hollow morphology.

Two types of silica including Stöber silica beads (SiO_2) and mesoporous silica spheres (MSS) (see TEM images of SiO_2 and MSS in Fig. S1 and/or Fig. 1a/Fig. 1i) were selected for this study. After several trial-and-error experiments, two successful approaches were realized to gain control over nickel-silicate synthesis by using each precursor. As shown in Fig. 1a-h, morphological variation of pristine SiO_2 bead with an excessive $mSiO_2$ (or CTAB-SiO_2) coating could lead to different shell thicknesses in the resultant product, whereas, according to Fig. 1i-l, the same MSS can be used to yield morphologically different nickel-silicate hollow sphere just by changing the base used.

According to our experimental findings, simply varying operational parameters such as temperature or hydrothermal treatment time could not efficiently control the shell thickness and the cavity size of metal-silicate hollow spheres. For instance, TEM images of NHS prepared from MSS at two different hydrothermal time does not show any tangible focal feature variation in terms of shell thickness (Fig. S2). However, it should be noted that temperature and time variation could lead to either a flawed or flawless transformation to a hollow morphology with an invariable shell thickness. Such observation in transformation of Stöber SiO_2 to metal-silicate hollow spheres were reported previously [9,19]. Therefore, to further engineer the hollow product, variation of the starting material architecture could be one possible formulation along with the previously reported reactants alteration procedures.

As shown in Fig. 1a,c,e,g, Stöber SiO_2 was coated with another $mSiO_2$ layer of varying thickness via a modified Stöber synthesis procedure using CTAB as a surfactant. Accordingly, three different SiO_2@CTAB-SiO_2 materials with varying the amount of TEOS were prepared, namely SCS0.1, SCS0.3, and SCS0.6 (Fig. 1c,e,g). When these SCS-based precursors used in hydrothermal transformation to NHS, the NHS products resulted with varying shell thickness ranging from ca. 10–100 nm (Fig. 1d,f,h). Comparably, the shell thickness of the final hollow nickel-silicate is approximately half of the $mSiO_2$ thickness in the respective SCSx sample (Fig. 1c-g,d-h). The size of hollow core in all samples remained equal (ca. 260 ± 20 nm). Interestingly, judging from TEM image of NiSiO-HS product produced form SCS0.6 (NHS-SCS0.6, Fig. 1h), it can be seen that a double-shelled hollow sphere is obtained.

Another synthetic route to obtain different shell thicknesses or altered inner cavity could be the use of different bases. Hitherto, two widely utilized bases such as NH_4OH and sodium acetate (CH_3COONa) are known as source of hydroxide ions in the transformation of pure Stöber SiO_2 to uniform metal-silicate hollow spheres of nickel-silicate, copper-silicate, etc. Applying these two bases separately during the transformation of pure Stöber SiO_2 to NHS have yielded the same product with a slight nuance in the external surface texture (Fig. S3). However, when the same protocol was repeated with a different silica precursor (i.e., MSS), the NHS product showed a different morphology. For example, in case of NH_4OH, a small-cavity compact-shell NHS (Fig. 1j) was obtained while for sodium acetate, a large-cavity thin-shell NHS (Fig. 1l) was resulted. In terms of chemical components, HRTEM-EDX elemental mappings and line-scan patterns of the corresponding products were acquired to demonstrate exact distribution of individual elements (Fig. S4), confirming that all the elements are evenly distributed across the hollow structure.

Furthermore, varying the ratio of NH_4OH to sodium acetate can provide additional adjustability of the NHS shell thickness along with hollowness by taking the combined effect of both bases (Scheme 1). As shown in Fig. 1j-k and S5, TEM images of the final products produced by varying the ratio of NH_4OH to sodium acetate confirmed this synthetic flexibility for making NHS materials. For example, when a base ratio of AS0.3 (where NH_4OH/SA equals to 2:0.3 v/v) is adopted (Fig. 1k and S5e,f), the intrinsic hollowness is expanded as compared to the situation when NH_4OH is solely used (Fig. 1j and S5a,b). By removing ammonia entirely, however, the hollowing effect is pronouncedly intensified
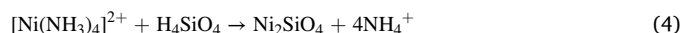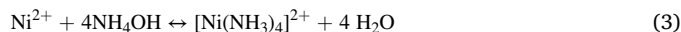
(Fig. 1l and S5g,h). Therefore, introducing more sodium acetate to the reaction medium thwart or suppress the NH_4OH effect leading to a product with thinner shell thickness.

Noting that complexation mechanism of Ni^{2+}, or in general transition metal cations, in the presence of each base is different, the followed reaction pathway of soluble nickel-silicate species (i.e., silicon-oxygen oligomers with different chain lengths) would also be different, yet an identical nickel-silicate phase (i.e., Ni_2SiO_4, Eqs. 4 and 6) is resulted [19]. The following are a few simplified steps for the product formation.
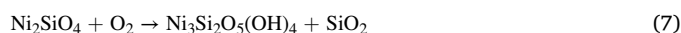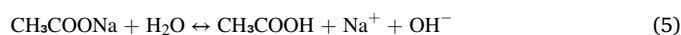
Hydrolysis of nickel sulfate and silica precursor:

$$SiO_2 + 2\ H_2O \leftrightarrow H_4SiO_4 \tag{1}$$

$$Ni(SO_4) \rightarrow Ni^{2+} + SO_4^{2-} \tag{2}$$

Nickel-silicate synthesis using NH_4OH:

$$Ni^{2+} + 4NH_4OH \leftrightarrow [Ni(NH_3)_4]^{2+} + 4\ H_2O \tag{3}$$

$$[Ni(NH_3)_4]^{2+} + H_4SiO_4 \rightarrow Ni_2SiO_4 + 4NH_4^+ \tag{4}$$

Nickel-silicate synthesis using sodium acetate:

$$CH_3COONa + H_2O \leftrightarrow CH_3COOH + Na^+ + OH^- \tag{5}$$

$$Ni^{2+} + H_4SiO_4 \rightarrow Ni_2SiO_4 + 4\ H^+ \tag{6}$$

$$Ni_2SiO_4 + O_2 \rightarrow Ni_3Si_2O_5(OH)_4 + SiO_2 \tag{7}$$

It should be noted that not all hydroxide precursors are effective for the same transformation. For instance, as shown in Fig. S6, when ammonium acetate is used as a base to prepare NHS from MSS, the final product was severely destructed in terms of shape and structure with just 1 mmol of the base used (Section 2.3).

To generalize the procedure to prepare other metal-silicates of various thicknesses using MSS, the nickel sulfate solution was replaced with other transition metal precursor solutions during the synthesis. The obtained metal-silicates (where metal is Fe, Cu, Co, and Zn) in the case of using both ammonia and sodium acetate as the bases can maintain their sphericity (Figs. S7 and S8), except for iron. In this particular case, both the bases (i.e., ammonia and sodium acetate) gave similar results (Figs. S7a-c and S8a,b).

For easy reference, Table 1 summarizes the sample labelling and synthesis conditions of different spherical hollow nickel-silicate samples prepared for this study.

3.2. Investigating the nature of as-synthesized NHS and their corresponding hydrogen-reduced samples

Table 2 lists the important characteristics of as-synthesized nickel-silicate hollow spheres (NHS) including the average diameter of the final hollow spheres, their shell thickness, and BET surface area. In addition, using the NHS as solid precursors, metallic Ni NPs can also be obtained on the surface or within the shell of each specimen upon hydrogen reduction, which will also be briefly examined in the following sections.

To confirm the common chemical nature of final nickel-silicates, FTIR and X-ray powder diffraction analyses were performed. As seen from FTIR spectra of all the as-synthesized NHS samples (Fig. 2a), most identical characteristic peaks of nickel-silicate phasic structure are identifiable at 1019 cm^{-1} (Ni–O–Si), 1077 cm^{-1} (Si–O–Si) along with other peaks located at 454 cm^{-1} (Si–O–Si), 666 cm^{-1} (O–Si–O), 706 cm^{-1} (δOH vibration in the nickel-silicate layer), and 799 cm^{-1} (Si–O) [9,19, 30–32]. According to the XRD patterns (Fig. 2b), all the samples also exhibited characteristic peaks of nickel-silicate hydrate (2θ ~26°, 36°, 61°, and 72°) and nickel-silicate (2θ ~25°; Ni_2SiO_4 shown in Eq. (4) & (6)) [9]. However, the latter XRD peak related to nickel-silicate may also have overlapping with amorphous silica phase which normally appears at 20–30° [19,33]. Comparing NHS-SiO_2-S and NHS-MSS-S XRD pattern, it is seen that the latter does not possess the broad peak at 20–30°,

Table 2

Textural characteristics of different as-prepared nickel-silicate hollow spheres.

Sample	As-synthesized					Reduced
	Hollow sphere diameter (nm)	Shell thickness (nm)	S_{BET} ($m^2.g^{-1}$)	Pore Volume[a] ($cm^3.g^{-1}$)	Pore Size[a] (nm)	Ni size (nm)
NHS-SiO₂-S	370	12	143.88	0.37	10.85	2.5 ± 0.6
NHS-SCS0.1-S	250	25	130.71	0.27	8.43	4.6 ± 0.7
NHS-SCS0.3-S	280	40	120.57	0.30	7.30	4.8 ± 1.0
NHS-SCS0.6-S	450	27 (77)**	116.78	0.23	7.39	4.8 ± 0.8
NHS-MSS-S	580	13	292.41	0.95	9.94	4.7 ± 1.4
NHS-MSS-AS0.3	380	115	140.46	0.24	5.53	6.8 ± 1.1
NHS-MSS-A	450	180	107.49	0.22	6.60	5.8 ± 0.7

[a] The values are calculated by Barrett−Joyner−Halenda (BJH) pore distribution based on desorption data.

** Distance between two shells in NHS-SCS0.6-S
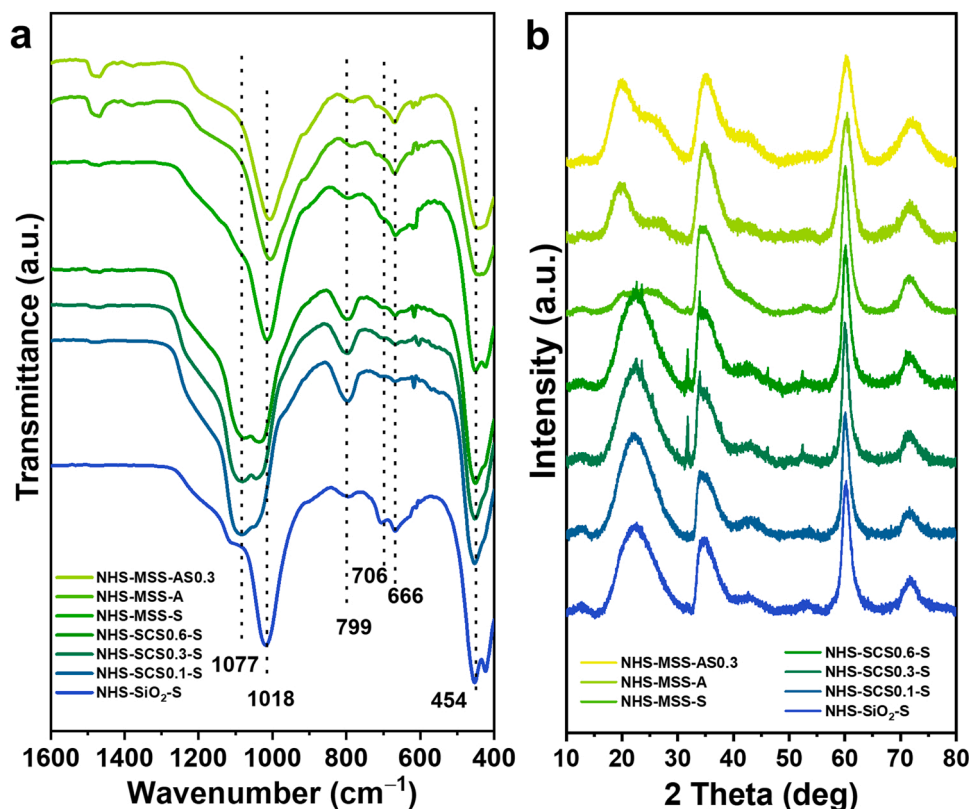
Fig. 2. (a) FTIR patterns and (b) XRD graphs of different as-synthesized nickel-silicate hollow spheres.
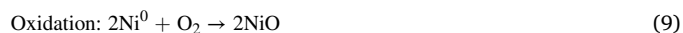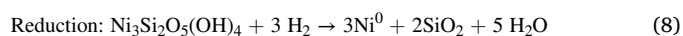
highlighting its weakened silica/silicate lattice.

N_2 adsorption-desorption analysis revealed the similarities and disparities of physiochemical properties of NHS products. Since, surface area could strongly affect the catalytic activity, Brunauer−Emmett−Teller (BET) surface area was quantified for all our samples. For the NHS samples derived from SiO_2 and SiO_2 coated with an external $mSiO_2$ layer, the BET specific surface area decreased by increasing the coating (Table 2). For instance, NHS-SiO₂-S has a surface area of 143.88 $m^2 \cdot g^{-1}$ while it is 116.78 $m^2 \cdot g^{-1}$ for NHS-SCS0.6-S. Furthermore, the Ni assay for all as-synthesized samples (except Ce-doped sample) was measured to be ~25 wt% by ICP-OES.

For nickel-silicate samples stemming from MSS and different bases, BET surface area decreases by changing the base from pure sodium acetate (NaCH₃COO) to pure NH₄OH due to variation in the final hollowness, while the base/alkaline combination showed a median value for BET surface area between the two limits. It is interesting to note that both pore volume and pore size have also followed the same decreasing trend as BET surface area for both MSS- and SiO₂-derived nickel-silicate samples. The N_2 isotherms of different samples and their corresponding

pore size distribution plots are provided in SI (Figs. S9 and S10).

Hydrogen-reduction of nickel-silicates was done to reduce their + 2 oxidation state to 0 (Eq. 8) in order to generate supported Ni NPs on silica within a morphologically-defined support [19].

$$\text{Reduction: } Ni_3Si_2O_5(OH)_4 + 3\,H_2 \rightarrow 3Ni^0 + 2SiO_2 + 5\,H_2O \quad (8)$$

$$\text{Oxidation: } 2Ni^0 + O_2 \rightarrow 2NiO \quad (9)$$

The reduced Ni NPs, on the other hand, can be readily oxidized into NiO phase on the surface of Ni NPs (Eq. 9) once being exposed to air. All the reduced samples are shown in Fig. 3 along with demonstrating their corresponding average Ni NPs size. The size of Ni NPs lies in the range of 4–6 nm for all hydrogen-reduced samples, except for NHS-SiO₂-S which is 2.5 nm. Moreover, better metal dispersion is visually seen for reduced NHS-SiO₂-S sample among all the samples (Fig. 3a). NHS-MSS-A and NHS-MSS-AS0.3 were found to have the largest Ni NPs sizes up to 6 nm, which may be ascribed to the involvement of ammonia in their preparative procedures. In addition to the role of ammonia, having the thickest shell for these two samples may explain the noticeable
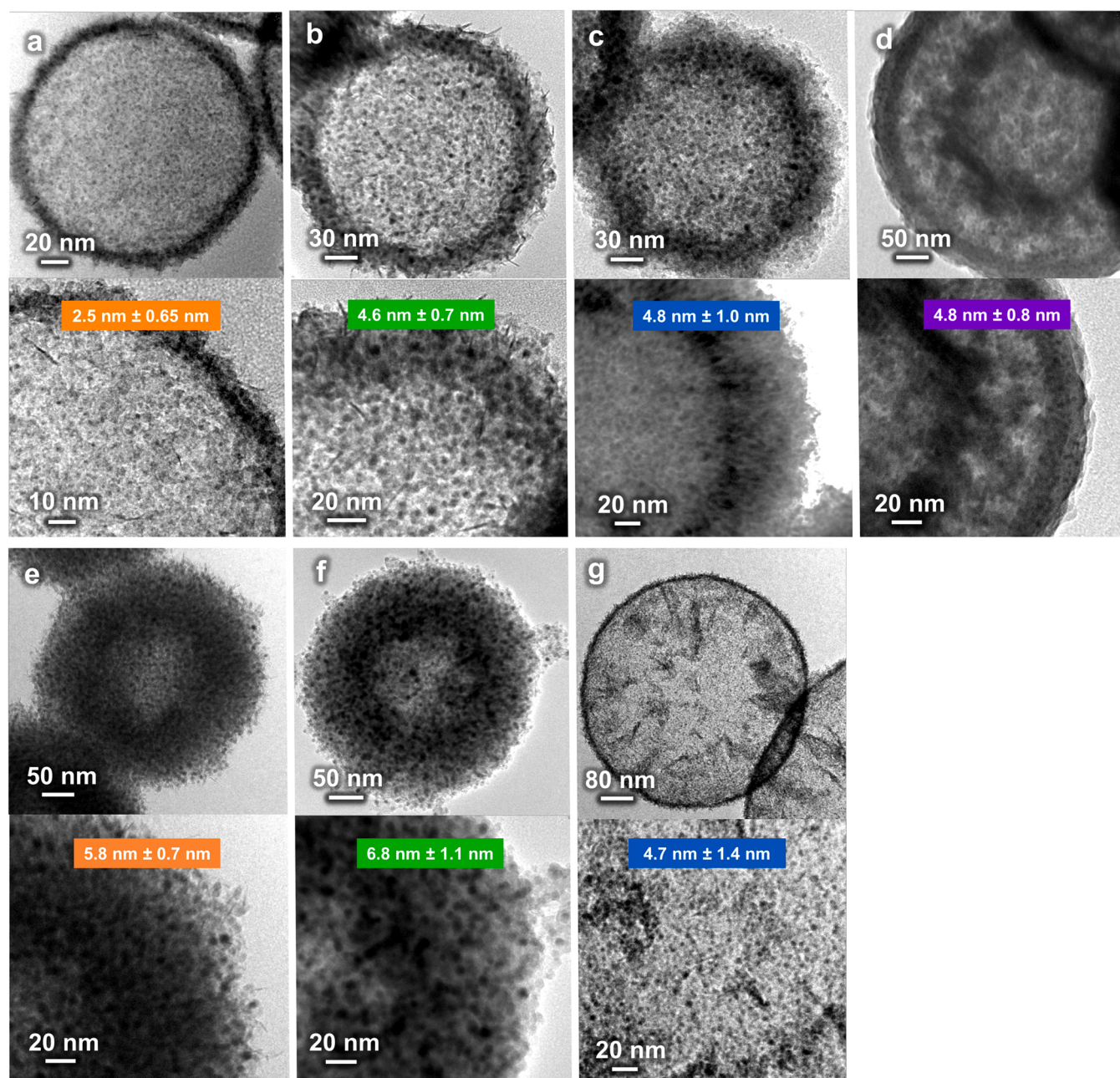
Fig. 3. TEM images at different magnifications of reduced NHSs (that is Ni/SiO$_2$ sphere) with mimicked morphology. H$_2$-reduced form of (a) NHS-SiO$_2$-S, (b) NHS-SCS0.1-S, (c) NHS-SCS0.3-S, (d) NHS-SCS0.6-S, (e) NHS-MSS-A, (f) NHS-MSS-AS0.3, and (g) NHS-MSS-S. The average size of Ni NPs for respective sample is shown on the respective TEM images according to their size distribution shown in SI (Fig. S11).

difference seen for Ni NPs size. The thinnest shell hollow sphere (i.e., NHS-MSS-S) demonstrates that its size of Ni NPs is even larger than that of NHS-SiO$_2$-S sample.

To investigate the reducibility of NHSs samples, H$_2$-TPR was conducted (Fig. 4). From H$_2$-TPR profiles, three main reduction peaks are identified for all the studied samples [34,35]. First, a low temperature reduction peak is located at ca. 200–450 °C attributing to the reduction of surface-formed NiO to metallic Ni. Second, a reduction peak located at 450–600 °C is ascribable to reduction of lattice Ni^{2+} cations in 1:1 nickel phyllosilicate (Ni PhyS) phase (Ni$_3$Si$_2$O$_5$(OH)$_4$) [19,32,36]. The third reduction peak at 690 °C could be related to the reduction of Ni^{2+} species of 2:1 Ni PhyS (Ni$_3$(Si$_2$O$_5$)$_2$(OH)$_2$) [32], which is the hardest species to reduce [36]. It is worthwhile to mention that for pure Ni supported on or contained inside SiO$_2$ supports (e.g., Ni@SiO$_2$), the third reduction peak (T > 690 °C) is not normally observed [37].

Nickel reduction of NHS-derived samples stemmed from Stöber SiO$_2$ and SCSx demonstrated that both hydrogen consumption and reduction temperature decrease by increasing the nickel-silicate shell thickness. This could be attributed to the presence of more 1:1 Ni PhyS phase (Ni$_3$Si$_2$O$_5$(OH)$_4$) as well as diffusion-limited reduction where hydrogen faces physical barrier during penetration into the center of the hollow spheres. Notably, the signal intensity for non-coating NHS-SiO$_2$-S sample is slightly higher than that of NHS-SCS0.6-S sample, implying higher hydrogen consumption for the former. On the contrary, for MSS-derived nickel-silicates, the reduction temperature decreases as the shell thickness varies from the thickest to the thinnest. However, hydrogen consumption is higher for a thinner nickel-silicate sample (e.g., NHS-MSS-S), because a thinner shell has a higher BET surface area (Table 2) and it is more accessible to hydrogen.
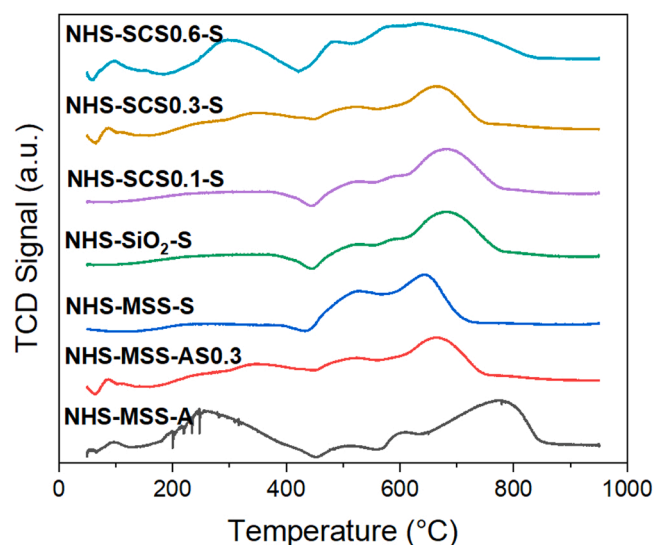
Fig. 4. H$_2$-TPR results for all nickel-silicate hollow spheres (NHS) samples studied in this work; also refer to TEM images of Fig. 3.

3.3. Evaluation of catalyst performance of nickel-silicate hollow spheres

Biogas reforming or DRM was selected to evaluate Ni/SiO$_2$ catalytic samples possessing different shell thicknesses (enforcing varied interior cavity and different Ni crystalline size) which all in all, could offer sintering resistance induced by the hollowing conformity. As detailed in Section 2.6, the biogas with a CH$_4$/CO$_2$ ratio of 1:1 and WHSV of 24 L·h^{-1}·g$_{cat}$$^{-1}$ was used at a temperature range of 400–750 °C.

Fig. 5 shows the CH$_4$ and CO$_2$ conversion and syngas ratio for all reduced nickel-silicate samples at 400–750 °C. As seen, for SiO$_2$-derived

hollow Ni/SiO$_2$ samples (Fig. 5a-c), their DRM performance decreases with increasing the coating thickness. Compared to NHS-SCS0.6-S, which exhibits the worst DRM performance, NHS-SCS0.1-S and NHS-SCS0.3-S samples are just slightly less active than NHS-SiO$_2$-S in terms of reactant conversion (X) and product molar ratio (H$_2$/CO). In general, it is seen that among these four samples, NHS-SiO$_2$-S and NHS-SCS0.1-S catalysts show the best performance, approaching theoretical thermo-dynamic conversion (H$_2$/CO = 1) at 750 °C and 0.1 MPa [38]. Furthermore, comparing the four samples, as the shell thickness of the nickel-silicate catalyst increases, the reaction performance decreases, mainly due to diffusion limitation caused by underdeveloped pores. Seo et al. showcased the same notion in which the mass transfer resistance increases with the shell thickness due to the underdeveloped pores [11]. When MSS-derived hollow Ni/SiO$_2$ samples are subjected to DRM (Fig. 5d-f), however, the sample with thickest shell (NHS-MSS-A) but a high porous nature displayed a good performance while the sample with the thinnest shell (NHS-MSS-S) exhibited the worst performance among all the samples, emanating from its weakened shell structure. It was deduced by other researchers that shell porosity could greatly influence the diffusion limitations to some extent [15].

A turning point at temperature of 500 °C is seen for some samples (marked by red arrows) for both CO$_2$ and CH$_4$ conversion curves in Fig. 5. Considering the fact that the consistent reduction treatment was performed for all the NHS samples prior to their reaction tests, this effect could be due to partial oxidization of the Ni NPs by CO$_2$ acting as a soft oxidant. However, with increase in temperature, the hydrogen produc-tion increases, causing in-situ activation of Ni NPs, leading to enhanced catalytic performance. Fig. S12 exhibits the CO$_2$ oxidation effect on Ni NPs proven by performing an in-situ CO$_2$ pulsing experiment chained between two H$_2$-TPR (before and after CO$_2$ pulsing experiment).

Concerning the H$_2$/CO ratio, a lower than unity value is normally resulted due to higher CO$_2$ conversion compared to CH$_4$ conversion and due to the occurrence of the reverse water gas shift reaction (RWGS)
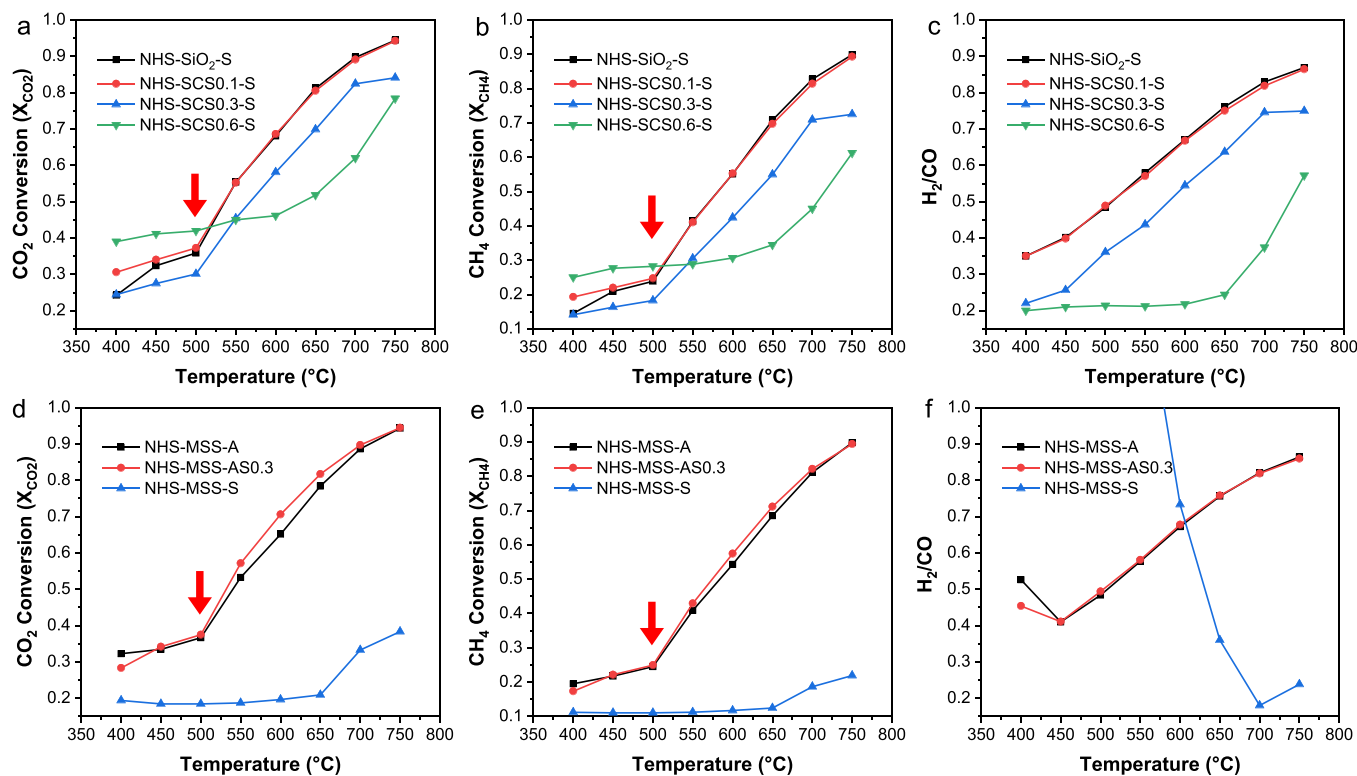

Fig. 5. DRM reaction results including CO$_2$ conversion (X$_{CO2}$), CH$_4$ conversion (X$_{CH4}$), and syngas ratio for reduced nickel-silicates samples. (a-c) NHS-SiO$_2$-S, NHS-SCS0.1-S, NHS-SCS0.3-S, and NHS-SCS0.6-S samples. (d-f) NHS-MSS-A, NHS-MSS-AS0.3, and NHS-MSS-S samples. Note: a turning point at 500 °C is pinpointed by a red arrow in some of the above plots.

simultaneously with DRM. According to our findings, under the condition of T = 750 °C and WHSV= 24 L/h.g$_{cat}$ applied during DRM, the best catalyst was found to be NHS-SiO$_2$-S (having the thinnest shell) with CO$_2$ and CH$_4$ conversion of 0.94 and 0.89, respectively. Under the same condition, this sample delivered a H$_2$/CO ratio of 0.77. This catalyst will be the basis for in-depth characterization of Ni NPs in the following sections.

3.4. Catalyst characterization

To understand the catalytic performance and their deactivation

chemistry, spent NHS-based catalysts were further evaluated by TEM, TGA, and XPS and compared with their fresh counterparts wherever needed. Special attention was also paid to the best catalyst (i.e., NHS-SiO$_2$-S) by extensive characterization using XPS, XANES, and in-situ DRIFTS analyses.

TEM images of the spent catalysts (Fig. 6), while observing no tangible shell-thickness expansion/contraction change for most of the catalysts after the reaction, revealed the existence of two major issues such as Ni NPs sintering and carbon deposition observed for some samples. While reduced SiO$_2$-derived NHS samples retained the size of Ni NPs with no major sintering, the increased shell coating resulted in
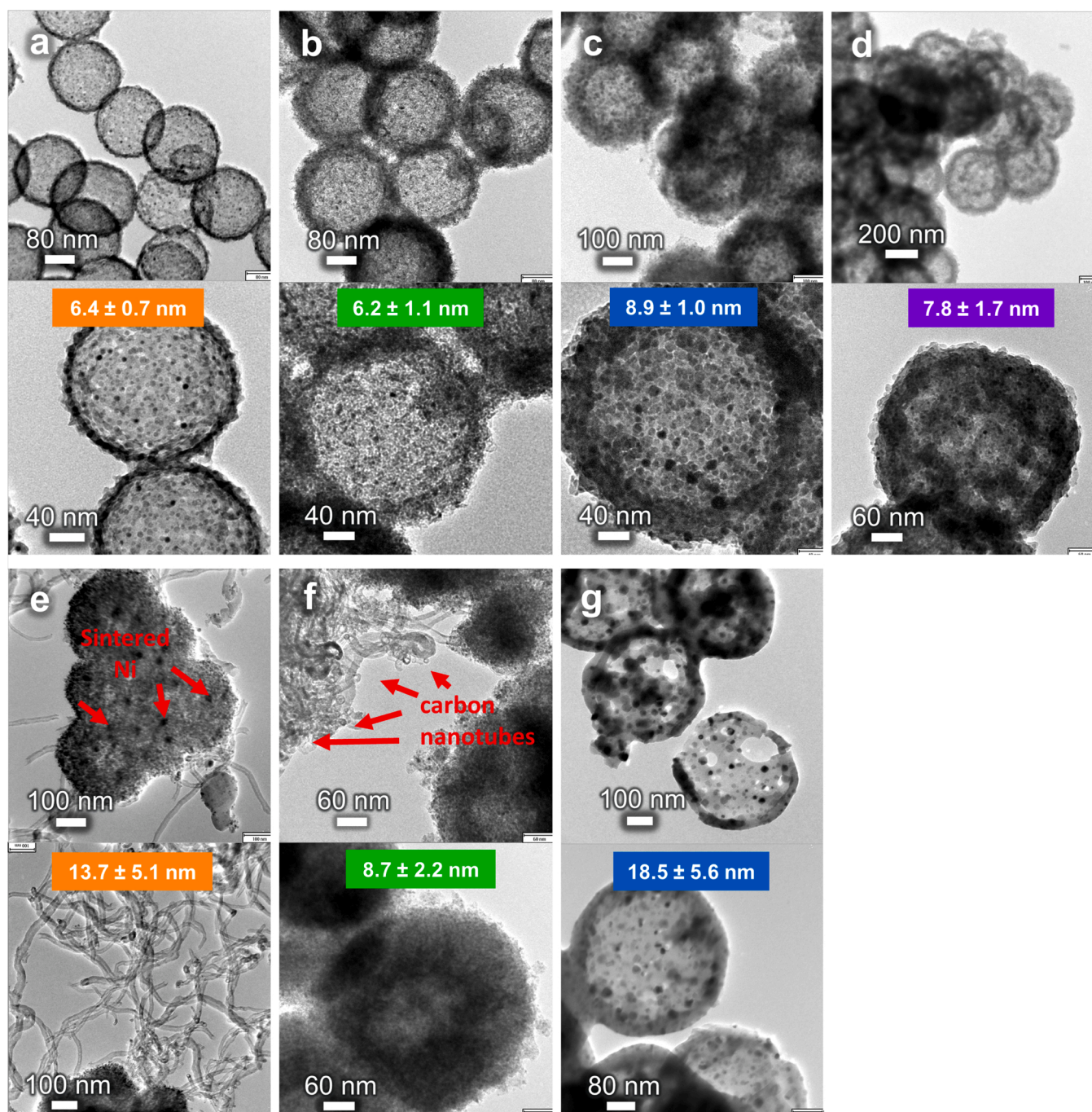
Fig. 6. TEM images of spent catalysts. (a) NHS-SiO$_2$-S, (b) NHS-SCS0.1-S, (c) NHS-SCS0.3-S, (d) NHS-SCS0.6-S, (e) NHS-MSS-A, (f) NHS-MSS-AS0.3, and (g) NHS-MSS-S. Notes: carbon formation in the form of multiwalled CNTs was only observed in NHS-MSS-A (e) and NHS-MSS-AS (f) samples. Sintered Ni NPs in (e) and nanocarbons in (f) are shown by red arrows, respectively. The average size of Ni NPs for the respective samples is provided together with the respective TEM images according to their size distribution shown in SI (Fig. S11).

slightly sintered Ni NPs in the catalysts after DRM reactions (Fig. 6a-d). Form the TEM images of respective spent catalysts of MSS-derived NHS samples (Fig. 6e-g), filamentous carbon formation was seen for NHS-MSS-A and NHS-MSS-AS0.3 (indicated with red arrows) whereas NHS-MSS-S demonstrated structure destruction after the reaction that explains its lower DRM performance (Fig. 5d-f). In this case, it should be mentioned that when the shell become too thin, the structure of NHS could be largely destroyed upon metallic nickel segregation under the reaction condition (Fig. 6g) as well as its partially developed silica and nickel-silicate lattice structures (Fig. 2b). Existence of large Ni particle size (>5 nm) within the thickest shell (180 nm for NHS-MSS-A) might be the reason to favor production of CNTs during DRM. Although carbon formation and Ni growth were seen for NHS-MSS-A sample, it still showed a good performance similar to that of the best sample (i.e., NHS-SiO$_2$-S), highlighting the effect of intensified shell porosity.

Carbon deposition was investigated for all spent hollow catalysts as well as Ni-SiO$_2$ (as a reference sample without any hollow core whose preparation is given in SI) using TGA analysis (Fig. S13). Quite interestingly, TGA of the SiO$_2$-derived spent catalyst samples (Fig. S13a) unraveled no weight loss upon heating up to 800 °C (meaning no carbon deposition). However, the two samples derived from MSS (i.e., NHS-MSS-A and NHS-MSS-AS0.3; Fig. 6e,f) having the largest shell thickness exhibited a drastic weight loss in the region of 500–660 °C which is due to the exothermic combustion of deposited coke [36]. Therefore, it is evinced that thin-shelled hollow samples are more effective against coke formation during DRM reaction performed at low WHSV values. When the reference Ni-SiO$_2$ sample with no hollow core was utilized in DRM, TGA analysis of its spent form (Fig. S13b) unveiled 83% weight loss due to its severe carbon deposition potentially arising from its morphology, which proves its incapability regarding coking hindrance. Such simple supported catalyst system also causes reactor blockage due to high carbon deposition [36].

The hollow spheres having the thickest shell demonstrated the growth of carbon nanotubes which could be attributed either to the facile movement of Ni NPs in the shell radial direction or to the ammonia utilization during their preparation. To further evaluate the carbon growth on ammonia-treated samples and the resistivity of Ni sintering in the best sample under harsher reaction environment, additional control experiments were performed by varying the reaction conditions and the catalyst parameters (Fig. S14). Accordingly, two WHSV values (2.5 and 5 times larger compared to the original WHSV used in Fig. 5) were evaluated for the thin-shell NHS-SiO$_2$-S catalyst (Fig. S14a,d). The ammonia-prepared thin-shell (NHS-SiO$_2$-A) sample was also tested if ammonia-treatment is responsible for Ni sintering and coking for the MSS-derived catalyst samples (Fig. S14g). These additional results showed that, as WHSV increases, hollow Ni/SiO$_2$ samples suffers from higher coking, however, no specific decrease in the reaction performance was observed. By increasing WHSV up to five times for example, the thin-shell Ni/SiO$_2$ suffers from higher carbon deposition (as revealed by TGA analysis in Fig. S14c,f) while no difference is seen between Ni NPs size (as revealed by TEM analysis in Fig. S14b,e).

Moreover, no difference is seen by varying the utilized base in the preparation of NHS from the same silica template (e.g., SiO$_2$ sphere). By evaluating the newly prepared thin-shelled NHS-SiO$_2$-A sample (Fig. S14g), it was revealed that ammonia-treatment for preparing initial nickel-silicate sample has no connection to the coke formation and Ni
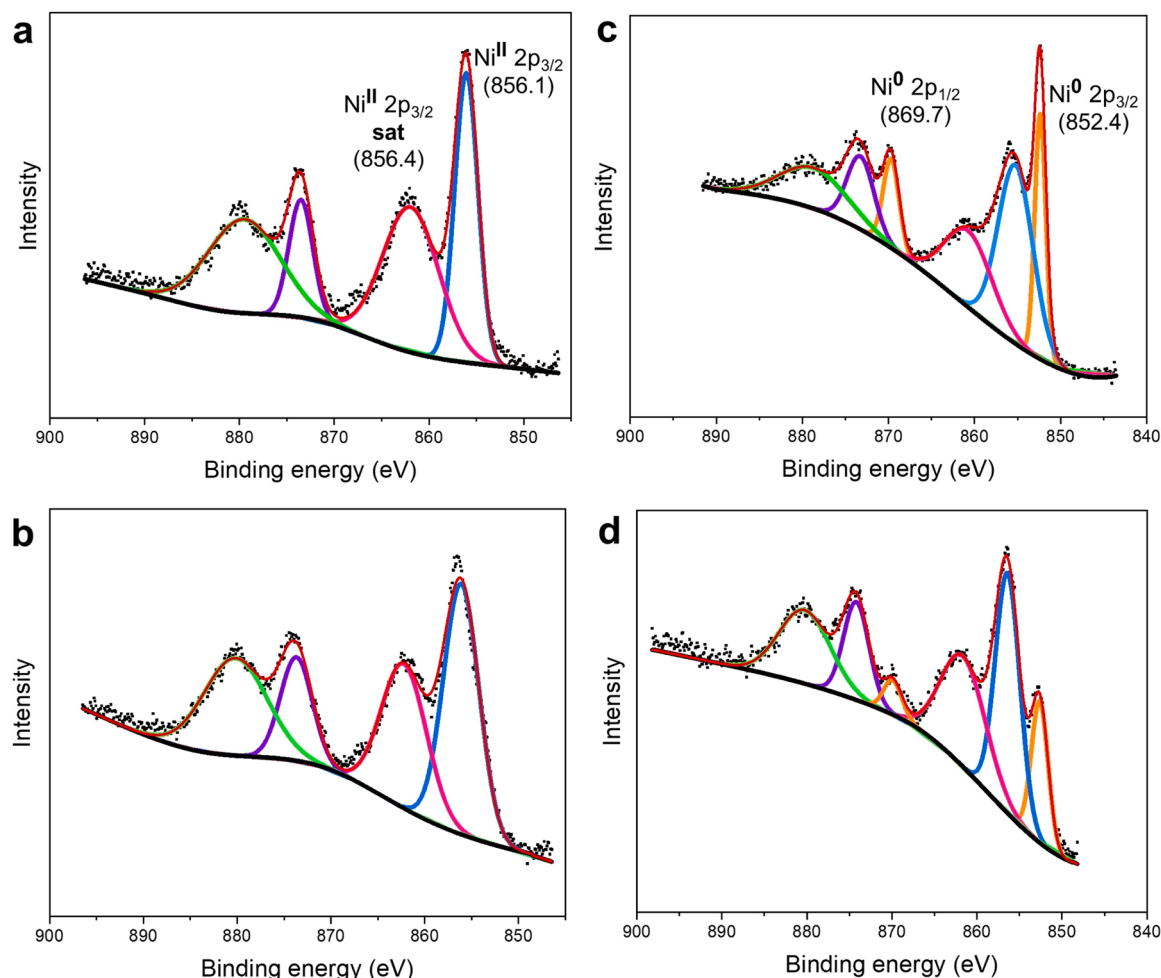

Fig. 7. Ni *2p* high-resolution XPS spectra for NHS-SiO$_2$-S sample in the form of (a) as-synthesized, (b) calcined, (c) reduced, and (d) spent catalyst.

sintering as no deposited carbon and sintered Ni particles were observed (Fig. S14h,i). Therefore, these control tests could further verify that a thin-shelled hollow SiO_2 catalyst with shell-confined Ni NPs could deliver reaction performance as high as possible along with withstanding the harsh reaction condition.

As XPS surface technique can probe into the sample surface up to a depth of 10 nm which is quite comparable to the shell thickness of nickel-silicate hollow sphere, the detected signal of imbedded Ni NPs could precisely reveal the surface chemistry of the catalyst as compared to other X-ray bulk-analysis techniques such as XRD and XAS. In Fig. 7, as-synthesized nickel-silicate hollow sphere shows strong signals of Ni^{2+} at 856.1 eV and its shakeup satellite at 856.4 eV (Fig. 7a). Compared to the as-synthesized sample, not much change in the XPS spectra was detected for air-calcined sample at 500 °C (Fig. 7b). As measured by XPS, after hydrogen reduction, a mixture of metallic Ni and Ni^{2+} was found on the surface, with the former being dominant (Fig. 7c). Ni^0 signal is located at 852.4 eV [39]. However, after the DRM reaction, Ni^0 signal intensity decreased while that of Ni^{2+} signal intensity increased (Fig. 7d), highlighting the oxidation of Ni surface species by either CO_2 or formed water. Such Ni oxidation also confirms retaining the small size of particles during the course of reaction since it is known that sintered Ni NPs with much larger size are less susceptible to oxidation [36]. The above analysis is valid because it is based on the comparison of relative peak intensities, despite the fact that nanoscale metallic nickel is also prone to ambient oxidation during the sample handling in XPS measurements.

To more precisely quantify the changes in the Ni chemical environment as well as validating the XPS results, XANES analysis was further explored. For extracting the XANES signals, after measuring absorption spectra and signal normalization, Athena software was used for the data reduction while Artemis software was used for shell fitting. XANES and EXAFS spectra are depicted in Fig. 8 and the structural parameters from the EXAFS fittings are listed in Table 3.

Fig. 8a shows the XANES absorption spectra for Ni K-edge for reference materials Ni foil (Ni^0), NiO (Ni^{2+}) and $Ni(OH)_2$ (Ni^{2+}) while R-space spectra of the corresponding samples are displayed in Fig. 8c. Ni K-edge absorption spectra were recorded for as-synthesized, calcined, reduced, and spent nickel-silicate hollow spheres (i.e., NHS-SiO_2-S) (Fig. 8b). As can be seen, XANES spectra of NiO and $Ni(OH)_2$ show a pre-edge peak and a white line at 8350.2 eV, whereas no white line and a weaker pre-edge is seen for Ni foil. For as-synthesized and calcined samples of NHS-SiO_2-S, an intensified white line intensity is seen, hinting to strong existence of Ni^{2+}. An attenuated white line intensity seen for the reduced NHS-SiO_2-S sample indicates that Ni^{2+} was not fully reduced to metallic Ni, corroborating the previous XPS results (Fig. 7). As noticed, after the DRM reaction, the spent NHS-SiO_2-S sample (as compared to its freshly reduced form) exhibited an even lower white line intensity but slightly stronger pre-edge peak, which is the result of partial Ni surface oxidation during the DRM reaction by CO_2 or formed water [36,40]. According to R-space graph (Fig. 8d), the calcined sample bond length for Ni–Ni oxide shell situated at 2.5 Å differs from its as-synthesized form (2.7 Å), resembling to that of R-space reference of NiO sample (2.55 Å) and showing the calcination effect on transforming nickel-silicate species to NiO structure.

While the reduced sample approximately follows the Ni foil R-space spectra, however, its EXAFS Fourier-transformed (FT) curve clearly demonstrates that much of the Ni bulk did not reduce properly, confirming our H_2-TPR results which showed that the 2:1 Ni PhyS phase

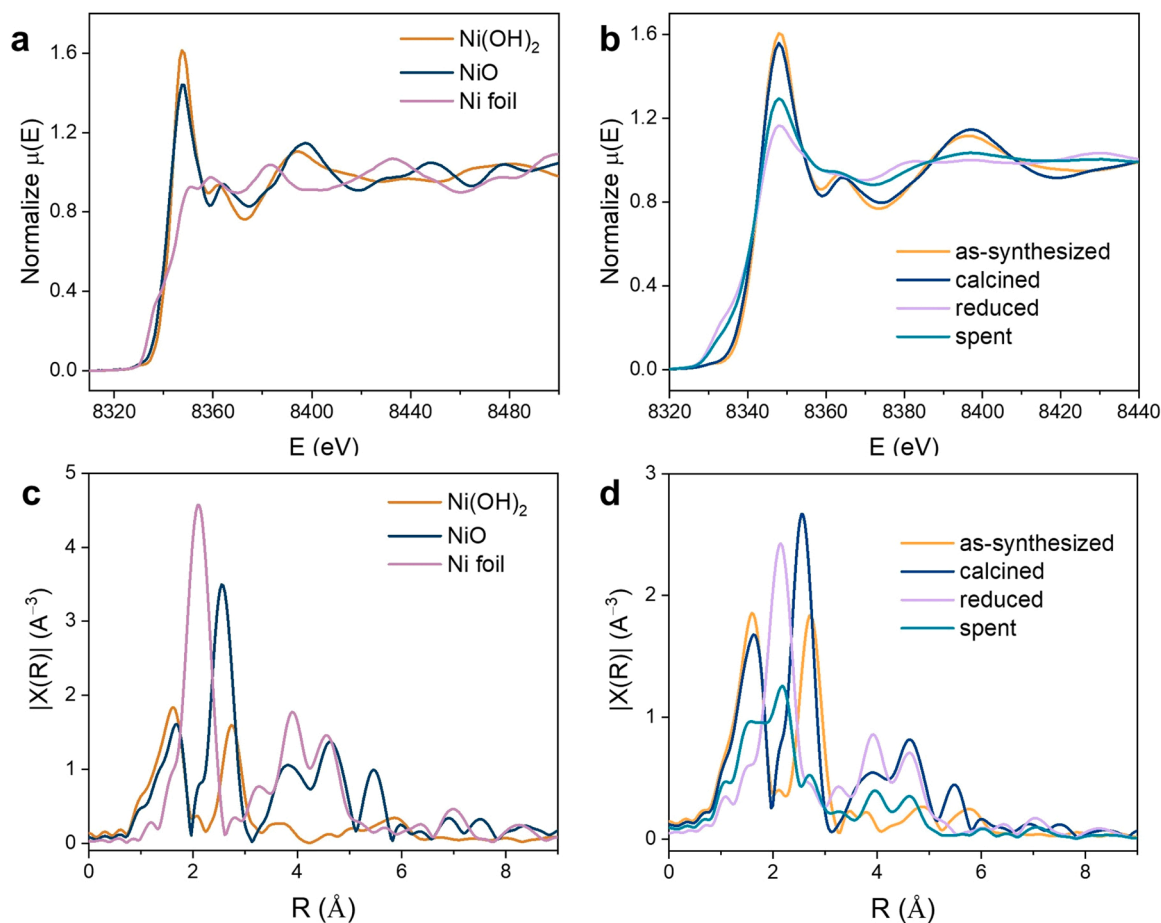**Fig. 8.** (a) Ni K-edge XANES spectra of reference samples of Ni foil, NiO, and $Ni(OH)_2$. (b) Ni K-edge XANES spectra of NHS-SiO_2-S sample in the forms of as-synthesized, calcined, reduced, and spent catalyst. (c, d) R-space EXAFS spectra of respective samples in (a) and (b).

Table 3

Structural parameters obtained by EXAFS fitting for NHS-SiO$_2$-S samples (in as-synthesized, calcined, reduced, and spent forms) and reference materials.

No.	Sample	Bond	R (Å)[a]	CN[b]	σ^2 (Å^2)[c]
1	Ni foil	Ni–Ni (m)	2.48 ± 0.04	12.0*	0.005
2	NiO	Ni–O (o)	2.09	6.0*	0.003
		Ni–Ni (o)	2.94 ± 0.34	6.0*	0.006
3	NHS-SiO$_2$-S (as-syn.)	Ni–O (o)	2.05 ± 0.02	6.1	0.007
		Ni–Ni (o)	3.08	6.4	0.008
		Ni–Si	3.26 ± 0.05	3.7	0.008
4	NHS-SiO$_2$-S (cal.)	Ni–O (o)	2.07 ± 0.02	5.7	0.007
		Ni–Ni (o)	2.09 ± 0.01	12.1	0.009
		Ni–Ni (m)	–	–	–
5	NHS-SiO$_2$-S (red.) (Ni/SiO$_2$)	Ni–O (o)	2.04 ± 0.05	2.5	0.004
		Ni–Ni (o)	3.04 ± 0.06	3.0	0.009
		Ni–Ni (m)	2.49 ± 0.01	2.3	0.005
6	Ni/SiO$_2$ (spent)	Ni–O (o)	2.49 ± 0.01	1.9	0.005
		Ni–Ni (o)	2.04 ± 0.01	7.1	0.006
		Ni–Ni (m)	–	–	–

[a] Bond distance in Angstroms;
[b] coordination number; [c] Debye-Waller factor;
*These values were fixed during EXAFS fitting, based on known structure of NiO and Ni foil.
Note: (m) stands for metallic shell, (o) stands for oxide shell.

(Ni$_3$(Si$_2$O$_5$)$_2$(OH)$_2$) is hard to reduce [36]. Expectedly, this might become even much more noticeable as the shell gets thicker. After the reaction, the spent sample showed an even intensified Ni–Ni metallic shell in the R-space EXAFS FT spectra at 2.12 Å which is due to the deep reduction of Ni species (confined in the shell) during the reaction by in-situ produced hydrogen via CH$_4$ dissociation. Furthermore, Table 3 gives the fitted structural parameters of bond type, coordination number (CN), bond length (R), and Debye-Waller factor (σ^2) for NHS-SiO$_2$-S sample under different stages of its preparation, calcination, reduction, and spent catalyst forms.

3.5. In-situ DRIFTS study

To understand the DRM reaction mechanism on the thinnest and thickest shell nickel-silicate hollow spheres, their intermediate surface species during the reaction were investigated and identified using in-situ DRIFTS technique (Fig. 9). FTIR spectra of reaction intermediates were collected on the surface of reduced catalyst by introducing a consistent flow of CO$_2$/CH$_4$ diluted with helium at elevated temperatures (Section 2.7). In general, characteristic peaks for reaction gases and main intermediates of DRM reaction including CO$_2$, CH$_4$, and CO as well as transient CO and carbonates could be found in the DRIFTS spectra [41].

3.5.1. In-situ DRIFTS analysis on NHS-SiO$_2$-S

The DRIFTS spectra of NHS-SiO$_2$-S (Fig. 9a) display peaks for gas phase CH$_4$ (3015 and 1304 cm^{-1}), gas phase CO$_2$ (2360 and 2340 cm^{-1}), and gas phase CO (a doublet peak in the range of 2170–2130 cm^{-1}). As noticed, CO peaks gets stronger as temperature increases, revealing the rise in conversion of CO$_2$ and CH$_4$. A weak peak at 2015 cm^{-1} at lower temperatures is assigned to linearly adsorbed CO on metallic Ni while other two weaker ones at 1950 and 1880 cm^{-1} are respectively ascribed to bridged and multi-centered CO on metallic Ni [42]. The increased

intensity of the 1880 cm^{-1} peak at increased temperature indicates that CO–Ni is the active intermediate in the DRM reaction. On the other hand, the low intensity of the linearly adsorbed CO peak on Ni surface indicates its less contribution to the reaction mechanism as well as the less surface affinity for its adsorption. The arrowed peaks in the spectra of reduced NHS-SiO$_2$-S are satisfactorily in line with the reported values for Ni supported on SiO$_2$ (Ni-SiO$_2$) [36]. Carbonate peaks are observable in the range of 1400–1600 cm^{-1} with two characteristic peaks at 1375 and 1595 cm^{-1} pertaining to the formate species [43]. Carbonyl bridged species, on the other hand, could be tracked from the appeared peaks at ca. 1800 and 1930 cm^{-1} [36]. A peak at 3744 cm^{-1} pertaining to OH group exhibits an increasing intensity with temperature elevation, highlighting consumption of the produced H$_2$ by parasitic RWGS reaction.

3.5.2. In-situ DRIFTS analysis on NHS-MSS-A

The presence of distinctive formate peak at 1350 cm^{-1}, lack of linear and bridged CO peaks, and disappearance of OH peak at 3744 cm^{-1} are the major disparities of the in-situ DRIFTS spectra of NHS-MSS-A sample (Fig. 9b) as compared to the NHS-SiO$_2$-S sample (Fig. 9a). It revealed that the former possessed the largest shell thickness leading to severely sintered Ni particles and depositing the highest coke after DRM reaction. This evidence might demonstrate the different reaction mechanism occurring due to morphological variants, that is mainly, the difference between how a thin-shelled hollow sphere with maximal inner cavity performs as compared to a thick-shell hollow sphere with minimal inner cavity. Similar to our observation, Xu et al. proposed that the porosity of a yolk-shell nanoreactor also played a significant role in the route selectivity of tandem reactions [16].

3.5.3. In-situ DRIFTS analysis by pulsing CH$_4$ and CO$_2$ on NHS-SiO$_2$-S

In DRM, numerous reactions may occur between all the adsorbed species. Depending on the catalyst composition and properties, the reaction mechanism may go through carbonate or formate intermediates as well as CH$_4$ and CO$_2$ stepwise dissociation, hence there is no specific reaction mechanism agreed on for DRM [44]. To get a better insight into the reaction mechanism as well as coke-resistivity due to morphological topology, DRIFTS analysis by alternately pulsing individual CH$_4$ and CO$_2$ gases on the freshly reduced NHS-SiO$_2$-S sample was conducted. Based on the reaction mechanism that reported for Ni-based catalysts, Ni sites dissociatively break adsorbed CH$_4$ into adsorbed carbon and H$_2$ either directly or via CH$_x$ intermediates (i.e., CH$_4$ to CH$_3$, CH$_3$ to CH$_2$, CH$_2$ to CH and finally, CH to C and H [45]), whereas adsorbed CO$_2$ on Ni sites is dissociated into adsorbed O and CO. The adsorbed O species subsequently reacts with the adsorbed carbon species to form another CO molecule. As shown in Fig. 9c, pulsing CH$_4$ alone on reduced NHS-SiO$_2$-S sample results in appearing a weak peak at 2360 cm^{-1} for gas phase CO$_2$, another weak peak at 2050 cm^{-1} for CO linear, and a broad peak at 1400–1500 cm^{-1} for carbonates. Compared to the carbonates peak which remained detected even after 5 min of CH$_4$ flow being switched off, the CO$_2$ and CO weak peaks are attenuating as time goes by. Although it is suggested that CH$_4$-derived carbonate species are oxidized to CO$_2$ on merely redox-capable highly active sites such as ceria (CeO$_2$), it could be inferred that a thin-shell Ni-contained silica with small-sized Ni NPs could act comparably to an active metal oxide phase [46]. From the disappearance of CH$_4$ peak (3015 cm^{-1}) after 5 min, it is conceivable that desorption process was not influenced by trapping species within the interior cavity of hollow sphere and thus there is no diffusion limitation (Fig. 9c). By flowing CO$_2$ followed by switching off CH$_4$ and flushing with helium (Fig. 9d), no change was observed except that CO$_2$ desorption occurs faster than that of CH$_4$ desorption within the same period. The carbonate peak intensity which was present after switching off CH$_4$ was not diminished after CO$_2$ gets off, demonstrating that carbonate could not be an active intermediate [36,47].

As seen from Fig. 9a, formate peak decreases by increasing temperature and fades beyond 450 °C and above, however does not fully
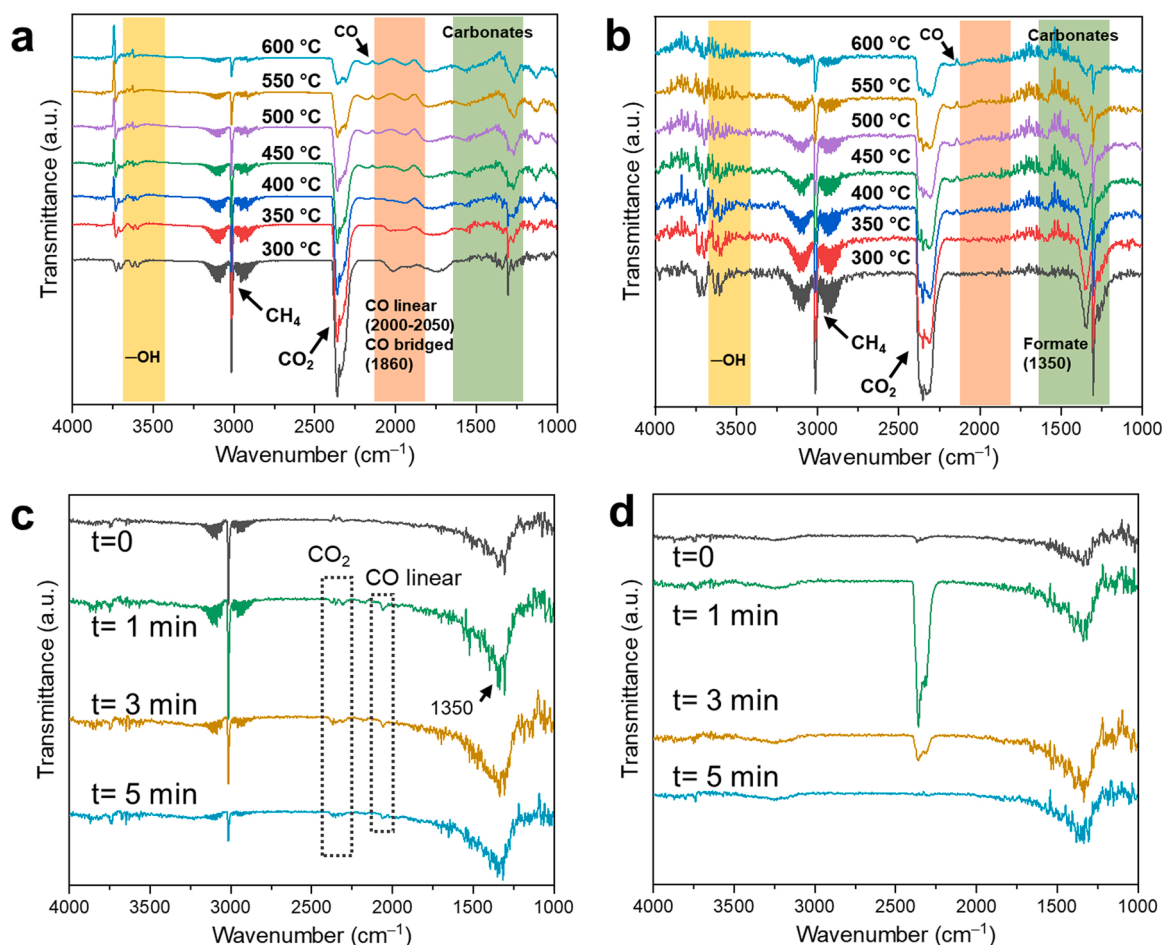
Fig. 9. Dry-reforming in-situ DRIFTS spectra for catalysts (a) NHS-SiO$_2$-S and (b) NHS-MSS-A. In-situ DRIFTS spectra for NHS-SiO$_2$-S sample at 500 °C by subsequent pulse introducing of (c) CH$_4$ and (d) CO$_2$.

disappear. Indeed, it still exists during the reaction, but at a lower intensity overlapping with the carbonate peak. From Fig. 9c, it is seen that formate peak appears at 1350 cm^{-1}, which sharpened at t = 1 min and diminished afterward. However, it is also not fully disappeared after CO$_2$ gets off. Thereof, it is also inferable that formate also could not be the active intermediate as compared to CO-derived and CH$_x$-related species [44].

3.6. Cerium doping into the NHS-SiO$_2$-S for inhibiting Ni sintering in DRM reaction

Besides outstanding morphological nature of hollow sphere nanocatalyst to effectively hinder Ni sintering during DRM such as Ni sequestration within sufficient reaction space or Ni containment within rigid mesoporous silica, metal-doping is another chemical modification pathway to overcome Ni sintering.

To appraise the effect of dopant addition onto the NHS interfaces for DRM reaction, a one-pot doping method was employed to prepare Ce-doped NHS-SiO$_2$-S [18]. As shown in Fig. 10a, HRTEM image and EDX-HRTEM elemental mappings of Ce-NHS-SiO$_2$-S sample exhibit both successful hollow morphology of the resultant sample as well as successful Ce inclusion and its uniform distribution within the hollow structure. According to XRD patterns of both NHS-SiO$_2$-S and Ce-doped NHS-SiO$_2$-S reduced samples (Fig. S15), it is obvious that after cerium doping, all characteristic metallic single-phase Ni peaks greatly suppressed especially the Ni XRD peak appeared at 45°.

Cerium doping into hollow nickel-silicate sphere structure, along with the maximized inner cavity suitable for coking inhibition acting as spatial hindrance for Ni sintering [20], can also further enhance Ni sintering resistivity, perhaps, at the cost of DRM catalytic performance. As reported, Ni sintering is largely inhibited in Ce-containing Ni-based catalysts due to the strong metal support interaction (SMSI) effect [48, 49], especially after reduction stage at high temperature, which may also contribute to attenuated activity of the catalyst.

High performing stability and low coke formation on Ce-doped NHS-SiO$_2$-S are expected because of the redox nature of the Ce NPs and Ni-Ce interface as well as cerium suppressing role on Ni particle size growth. According to the DRM catalytic performance of Ce-doped NHS-SiO$_2$-S at lowest employed WHSV value (Fig. 10b), it is seen that both CO$_2$ and CH$_4$ conversions are exactly equivocal to that of same sample without Ce dopant. This might be attributed to the presence of adequate Ni sites to facilitate the reaction at such diluted reaction medium per Ni content due to a low WHSV. However, syngas ratio is slightly lower for Ce-doped sample as compared to that without Ce dopant (i.e., H$_2$/CO is 0.859 for the former and 0.869 for the latter at 750 °C). When a higher WHSV applied (Fig. 10c), both CH$_4$ and CO$_2$ conversions experienced a dramatic decrease of nearly 10–25% in all tested temperatures as compared to NHS-SiO$_2$-S sample. For instance, at 750 °C (and WHSV = 120 L·h^{-1}·g$_{cat}$$^{-1}$), Ce-doped NHS-SiO$_2$-S catalytic results (X$_{CO2}$ = 0.67 and X$_{CH4}$ = 0.53) are tangibly lower than that of NHS-SiO$_2$-S catalytic results (X$_{CO2}$ = 0.80 and X$_{CH4}$ = 0.69). Nevertheless, the coke resistivity of the former is significantly better than the latter as revealed from TGA analysis of their spent catalysts (Fig. S16). Accordingly, for both WHSV (i.e., 24 and 120 L·h^{-1}·g$_{cat}$$^{-1}$) applied for the Ce-doped sample, no perceptible weight loss was detected (Fig. S16a,b) while for the NHS-SiO$_2$-S sample at higher WHSV, 30% weight loss was observed
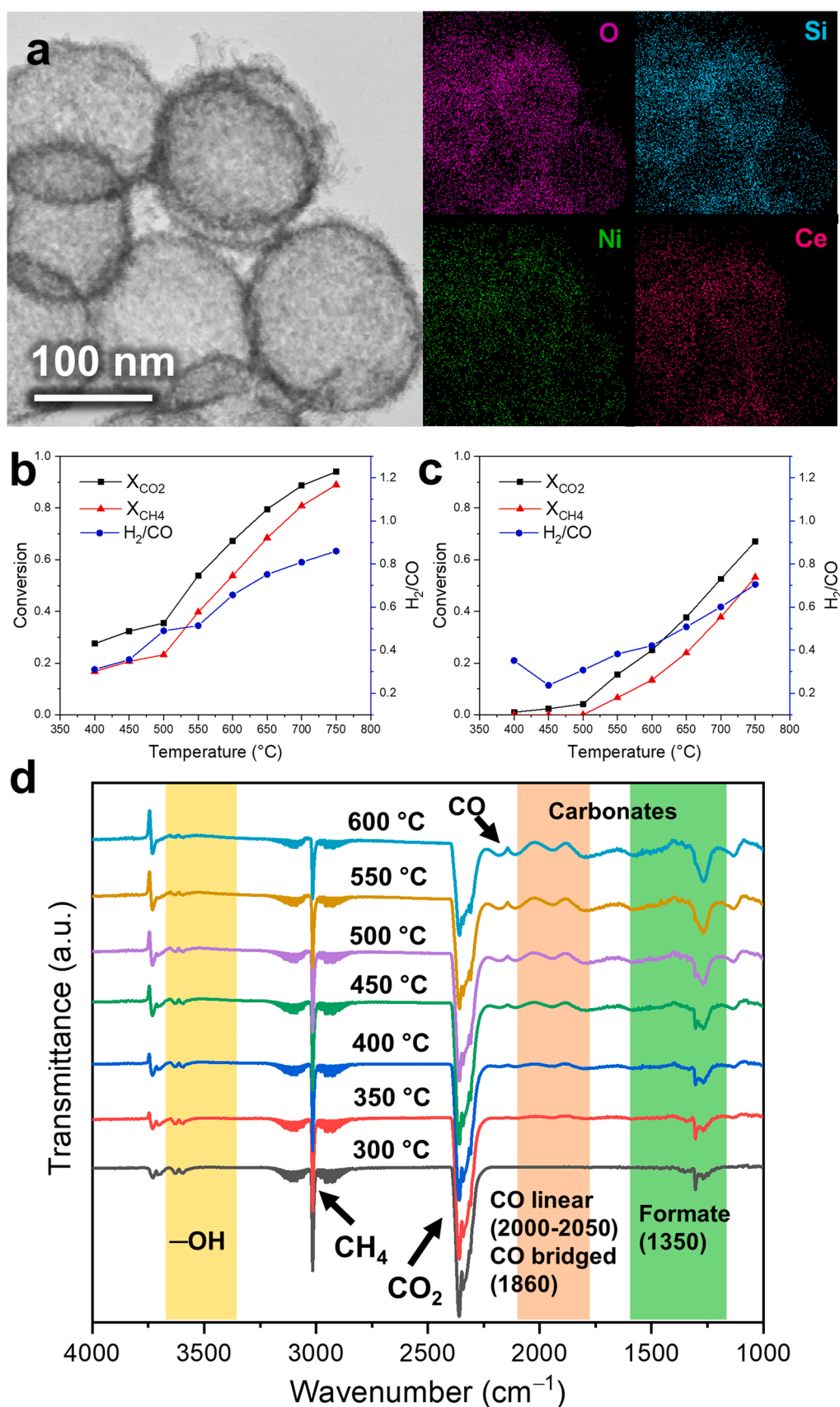
Fig. 10. (a) Ce-doped NHS-SiO$_2$-S HRTEM image and the respective HRTEM-EDX elemental mappings for Ni, Ce, O, and Si. DRM reaction data of Ce-doped NHS-SiO$_2$-S for (b) WHSV= 24 L·h^{-1}·g$_{cat}$$^{-1}$ and (c) WHSV= 120 L·h^{-1}·g$_{cat}$$^{-1}$. (d) In-situ DRIFTS result for Ce-doped NHS-SiO$_2$-S sample.

(Fig. S14f). This might also suggest a change in the reaction mechanism pathway, which needs to be investigated using in-situ DRIFTS.

The reaction mechanism for Ni-CeO$_2$ supported on SiO$_2$ may follow a bifunctional redox pathway instead of a mono-functional one [36]. Accordingly, both Ni and Ni-CeO$_2$ interfaces are responsible for dissociations of CH$_4$ and CO$_2$ with intensified role of oxygen vacancies (O$_x$) acting as adsorption and activation sites. As illustrated in Fig. 10d, DRIFTS spectra of Ce-doped NHS-SiO$_2$-S sample evidently demonstrate presence of both CO-intermediates (i.e., CO-linear and CO-bridged) as well as carbonate-intermediate whose intensity is increased by increasing the temperature. At a high temperature of 600 °C, in-situ DRIFTS spectra of NHS-SiO$_2$-S (Fig. 9a) containing small-sized Ni NPs on a thin-shell hollow sphere feature intensified CO-intermediate but attenuated carbonates-intermediates while that of NHS-MSS-A (Fig. 9b) containing large-sized Ni NPs on a thick-shell hollow sphere feature intensified carbonates-intermediates but attenuated CO-intermediate. However, it is seen for Ce-doped NHS-SiO$_2$-S sample that both CO-intermediate and carbonates-intermediates have intensified signals during the dry-reforming. Therefore, this proves the change occurred in the reaction mechanism from a mono-functional redox pathway to a bi-functional one where highly active lattice oxygen vacancies induced upon Ce-doping chiefly lower CO$_2$ adsorption on Ni sites and reduce CO$_2$ content to CO indirectly. Finally, Ni-CO species by CO$_2$ dissociation cannot be produced on Ce-doped sample since CO$_2$ is not dissociated on Ni sites on this sample.

3.7. Stability of hollow spheres during DRM reaction

The stability of hollow spheres within a reaction is highly important to consider them as pragmatically relevant catalysts. Fig. S17 shows the stability test for NHS-SiO$_2$-S and Ce-doped NHS-SiO$_2$-S samples for DRM reaction at 750 °C. The stability test for these hollow spheres was conducted under the harshest reaction condition (biogas flowrate = 100 mL·min^{-1} and T = 750 °C) with a CH$_4$:CO$_2$ ratio of 1:1 for 50 h time-on-stream (TOS).

Although initial reactivity for NHS-SiO$_2$-S catalyst was higher than that of Ce-doped NHS-SiO$_2$-S catalyst, but NHS-SiO$_2$-S showed a higher decreasing reactivity trend (Fig. S17). Moreover, during 50 h TOS, H$_2$/CO ratio was started at 0.50 and ended at 0.40 for NHS-SiO$_2$-S while it was quite stable for Ce-doped NHS-SiO$_2$-S sample (remained plateau at ca. 0.5). Therefore, Ce-doping could stabilize the catalyst performance and prevent its catalytic reactivity attenuation. Regarding the syngas ratio, NHS-SiO$_2$-S catalyst experienced an attenuation in H$_2$/CO ratio while Ce-doped NHS-SiO$_2$-S catalyst exhibited a plateau of H$_2$/CO curve during 50 h TOS. However, Ce-doped sample performance was slightly lower than that of NHS-SiO$_2$-S, similar to an earlier report [36]. Furthermore, no reactor blocking problem was observed for both catalysts over the whole TOS. This is interesting since problematic coke formation is normally excepted for common Ni-SiO$_2$ samples [36], except those that leverage on architectural advantage [21].

3.8. Comparison of different catalysts for DRM reaction from this work and literature

DRM reaction performance (i.e., CO$_2$ and CH$_4$ conversion and resulted syngas ratio) was compared for different Ni-based structure-different catalysts reported in the literature and the hollow morphologies developed in this work. The results of our work for different samples are listed in Table 4 while the literature data are presented in Table 5. Although by no means this should be considered as a holistic comparison, however, it would provide interesting analogies.

Based on the data, most of the compared works exploited morphology optimization to study the DRM reaction performance and Ni behavior. However, as seen, our nickel-silicate hollow spheres, especially NHS-SiO$_2$-S (Table 5), have shown the highest performance (i.e., biogas conversion) among various reported works. As compared to the performance of NHS-SiO$_2$-S, Ni/SBA-EG [53] and Ni@SiO$_2$ [57] displayed higher nominal conversions of CO$_2$ and CH$_4$ in which the former utilized the same WHSV but at a reaction temperature of 50 °C higher and the latter was at the same reaction temperature but at a lower WHSV. As known, metal-metal oxide interface, Ni chemical environment, Ni particle size, metal distribution, promoter, adjusted Ni content, and metal-support interaction are more prominent factors for this reaction. Nevertheless, from Table 5, it is seen that DRM performances of Ni-contained samples with different morphological design and architectural topology are all quite acceptable or even remarkable in some cases. Therefore, this proves the advantages of morphology optimization during the catalytic design and engineering consideration. Even as compared to promoter-enhanced catalysts such as Ni/SBA16 Ce-doped (Table 5) [54], our hollow spheres of Ce-doped NHS-SiO$_2$-S catalyst demonstrated better CO$_2$ and CH$_4$ conversion of 94% and 89% even at a higher WHSV value with no coke formation.

With the highest WHSVs reported so far for dry-reforming such as 1524 and 200 L·h^{-1}·g$_{cat}$$^{-1}$, CH$_4$ conversions of 11% and 51% were reported, respectively [50,56]. In comparison, for a WHSV = 120 L·h^{-1}·g$_{cat}$$^{-1}$ at 750 °C, both NHS-SiO$_2$-S and Ce-doped NHS-SiO$_2$-S rendered CH$_4$ conversion equal to 69% and 53%, which are still quite comparable to such outstanding literature data for low Ni-loaded catalysts. CH$_4$ specific activity (S.A.$_{CH4}$) values are respectively found to be 0.1 and 0.11 for NHS-SiO$_2$-S and Ce-doped NHS-SiO$_2$-S samples.

As implied by the results of our study, the hollow morphology of our NHS catalyst manifests salient morphological features such as thin-to-thick shell (determining distribution of metal content across the shell), a natural curvature conformation, and a maximized inner cavity. These features could then demonstrate the importance of the morphology effect on the catalytic activity during a chemical reaction, known as morphology-performance relationship.

4. Conclusion

In summary, versatile hollow nickel-silicate spheres with thin-to-thick shell thickness and minimal-to-maximal inner cavity were

Table 4

DRM catalytic results (CO$_2$ & CH$_4$ conversions, CO$_2$ & CH$_4$ specific activities, H$_2$/CO ratio) of different catalysts from this work.

Catalyst	X$_{CO2}$ (S.A.$_{CO2}$)	X$_{CH4}$ (S.A.$_{CH4}$)	H$_2$/CO	WHSV (L/h.g$_{cat}$)	Temp. (°C)	TGA$_{Coke}$ (wt%)
NHS-SiO$_2$-S	0.94	0.89	0.87	24	750	0
NHS-SCS0.1-S	0.94	0.89	0.86	24	750	0
NHS-SCS0.3-S	0.84	0.72	0.74	24	750	0
NHS-SCS0.6-S	0.78	0.61	0.57	24	750	0
NHS-MSS-S	0.38	0.21	0.23	24	750	0
NHS-MSS-AS0.3	0.94	0.89	0.89	24	750	35
NHS-MSS-A	0.94	0.89	0.85	24	750	26
NHS-SiO$_2$-S	0.91	0.85	0.85	60	750	12
NHS-SiO$_2$-S	0.80 (0.12)	0.69 (0.10)	0.77	120	750	30
NHS-SiO$_2$-A	0.94	0.89	0.86	24	750	0
Ce-doped NHS-SiO$_2$-S	0.94	0.88	0.85	24	750	0
Ce-doped NHS-SiO$_2$-S	0.67 (0.14)	0.53 (0.11)	0.70	120	750	5

Table 5

DRM catalytic comparison table for different catalysts from this work with that of literature.

Catalyst	X_{CO2} (S.A.$_{CO2}$)	X_{CH4} (S.A.$_{CH4}$)	H_2/CO	WHSV (L/h.g_{cat})	Temp. (°C)	TGA$_{Coke}$ (wt%)	Ref.
NHS-SiO$_2$-S	0.80 (0.12)	0.69 (0.10)	0.77	120	750	30	**This work**
Ce-doped NHS-SiO$_2$-S	0.67 (0.14)	0.53 (0.11)	0.70	120	750	5	**This work**
Ni/SiO$_2$@CeO$_2$	0.89 (0.50)	0.51 (0.40)	0.90	200	750	0	[36]
Ni@SiO$_2$	0.71 (nil)	0.57 (0.02)	0.48	48	750	1.2	[50]
Ni@SiO$_2$	0.26 (nil)	0.11 (0.09)	0.48	1524	750	1.2	[50]
Ni@Ni-SiO$_2$ yolk-shell	0.82 (0.59)	0.74 (0.41)	0.90	1.44	800	9	[51]
Ni@SiO$_2$ nanocapsule	0.80 (0.13)	0.73 (0.11)	0.95	60	700	1.5	[20]
SiO$_2$@Ni@SiO$_2$ multicore-shell	0.59 (0.23)	0.49 (0.19)	0.78	60	800	7.6	[52]
Ni/SBA15-EG	0.96 (nil)	0.87 (0.04)	nil	24	800	3.8	[53]
Ni/SBA16 Ce-doped	0.77 (0.23)	0.73 (0.16)	0.73	12	700	3.8	[54]
Ni/SiO$_2$@SiO$_2$	0.62 (1.07)	0.36 (0.63)	0.65	12	800	nil	[55]
Ni-SiO$_2$ (10% Ni)	nil (nil)	0.80 (0.11)	nil	144	800	0	[56]
Ni@SiO$_2$	0.95 (0.14)	0.90 (0.13)	1.03	18	750	0.7	[57]
Ni/SiO$_2$ nanofiber	0.78 (0.06)	0.63 (0.05)	0.95	48	700	10	[58]
Ni@SiO$_2$ core-shell (14.6% Ni)	0.90 (0.03)	0.77 (0.03)	0.99	18	750	0.5	[37]
Ni@SiO$_2$ core-shell (6.1% Ni)	0.87 (0.08)	0.80 (0.07)	0.91	18	750	0	[37]

successfully synthesized by employing two different strategies of precursor morphology optimization and operational parameter adjustment. Under the first protocol, Stöber silica (or SiO$_2$) beads coated with additional layers of modified Stöber silica (or mesoporous silica or in short *m*SiO$_2$) with different thicknesses were exposed to a one-pot hydrothermal procedure in the presence of nickel sulfate and sodium acetate. As a result, final hollow nickel-silicates exhibited varied shell thicknesses from a 11 nm up to a double-shell morphology with 77 nm being the inner shell distance. Under the second protocol, a mesoporous silica spheres (or MSS) prepared from an oil-water emulsion were used during the hydrothermal procedure as the silica source but with different base sources changing from sodium acetate to ammonia. By virtue of that, a varied inner cavity changing was observed with size of the shell thickness ranging from 13 nm to 180 nm. Upon reduction of prepared nickel-silicate samples which possess a relatively high Ni assay (~30%), Ni^0/SiO$_2$ is obtained.

To uncouple the distinctive disparities between the salient morphological features of such resultant catalytic hollow spheres, their catalytic performance was evaluated for model gas-phase reaction of syngas synthesis from biogas (known as dry reforming of methane or DRM). Biogas (CH$_4$/CO$_2$ = 1) reforming at different temperatures ranging from 400° to 750°C for all samples at low reaction gas flow rate exhibited full thermodynamic conversion for both CO$_2$ and CH$_4$. However, by increasing the shell thickness for SiO$_2$-derived samples, a decreasing CO$_2$ and CH$_4$ conversion trend was observed. Quite interestingly, no coke formation realized during the reactivity tests. For MSS-derived samples having the thickest shell thickness when treated with ammonia and the thinnest shell thickness when treated with sodium acetate, whisker carbon growth and morphology destruction were found to be the problematic issues. Overall, nickel-silicate derived from pure Stöber silica (i.e., NHS-SiO$_2$-S) sample was found to perform satisfactorily among different samples, highlighting the importance of maximal inner cavity, a conducive thin shell with a fairly robust structure, and a highly curved conformation. However, due to possible sintering of metallic nickel in the resultant structure under the high-WHSV DRM reaction condition and to further boost its coking-resistivity, the high Ni content NHS-SiO$_2$-S was doped with cerium to yield Ce-doped NHS-SiO$_2$-S. The doped catalyst performance was comparable at lower biogas WHSV and negligibly lower at higher biogas WHSV, yet with greater coking suppression, compared to NHS-SiO$_2$-S sample.

Author contribution

M. Kosari conceived the idea, conducted most of the experimental work, data analysis and interpretation, and composed the manuscript. S. Askari did the DRIFTS and TPR experiments under S. Kawi supervision. X. Shibo carried out XAS experiments and revised the XAS part. A.M.

Seayad supervised data analysis, curation and interpretation, and revised the manuscript. A. Borgna and H.C. Zeng conceived the project idea, supervised the research implementation, data analysis, curation and interpretation, and reviewed and revised the manuscript.

Declaration of Competing Interest

The authors declare that they have no known competing financial interests or personal relationships that could have appeared to influence the work reported in this paper.

Appendix A. Supporting information

Supplementary data associated with this article can be found in the online version at doi:10.1016/j.apcatb.2022.121360.

References

[1] B. Li, H.C. Zeng, Architecture and preparation of hollow catalytic devices, Adv. Mater. 31 (2019), 1801104.

[2] M. Kosari, A. Borgna, H.C. Zeng, Transformation of stöber silica spheres to hollow nanocatalysts, ChemNanoMat 6 (2020) 889–906.

[3] D. Yao, Y. Wang, K. Hassan-Legault, A. Li, Y. Zhao, J. Lv, S. Huang, X. Ma, Balancing effect between adsorption and diffusion on catalytic performance inside hollow nanostructured catalyst, ACS Catal. 9 (2019) 2969–2976.

[4] A.M. Lim, H.C. Zeng, Antisolvent route to ultrathin hollow spheres of cerium oxide for enhanced CO oxidation, ACS Appl. Mater. Interfaces 13 (2021) 20501–20510.

[5] P. Jin, Q. Chen, L. Hao, R. Tian, L. Zhang, L. Wang, Synthesis and catalytic properties of nickel–silica composite hollow nanospheres, J. Phys. Chem. B 108 (2004) 6311–6314.

[6] P. Xu, R. Yu, H. Ren, L. Zong, J. Chen, X. Xing, Hierarchical nanoscale multi-shell Au/CeO$_2$ hollow spheres, Chem. Sci. 5 (2014) 4221–4226.

[7] J. Chen, D. Wang, J. Qi, G. Li, F. Zheng, S. Li, H. Zhao, Z. Tang, Monodisperse hollow spheres with sandwich heterostructured shells as high-performance catalysts via an extended SiO$_2$ template method, Small 11 (2015) 420–425.

[8] J. Guan, X. Pan, X. Liu, X. Bao, Syngas segregation induced by confinement in carbon nanotubes: a combined first-principles and Monte Carlo study, J. Phys. Chem. C 113 (2009) 21687–21692.

[9] C.C. Yec, H.C. Zeng, Nanobubbles within a microbubble: synthesis and self-assembly of hollow manganese silicate and its metal-doped derivatives, ACS Nano 8 (2014) 6407–6416.

[10] C. Wang, H. Wu, X. Jie, X. Zhang, Y. Zhao, B. Yao, T. Xiao, Yolk–shell nanocapsule catalysts as nanoreactors with various shell structures and their diffusion effect on the CO_2 reforming of methane, ACS Appl. Mater. Interfaces 13 (2021) 31699–31709.

[11] M.-g Seo, H.J. Kim, S.S. Han, K.-Y. Lee, Effect of shell thickness of Pd core-porous SiO_2 shell catalysts on direct synthesis of H_2O_2 from H_2 and O_2, J. Mol. Catal. A: Chem. 426 (2017) 238–243.

[12] L. Zhang, J. Lian, L. Li, C. Peng, W. Liu, X. Xu, X. Fang, Z. Wang, X. Wang, H. Peng, $LaNiO_3$ nanocube embedded in mesoporous silica for dry reforming of methane with enhanced coking resistance, Microporous Mesoporous Mater. 266 (2018) 189–197.

[13] B. Zeng, B. Hou, L. Jia, J. Wang, C. Chen, D. Li, Y. Sun, The intrinsic effects of shell thickness on the Fischer–Tropsch synthesis over core–shell structured catalysts, Catal. Sci. Technol. 3 (2013) 3250–3255.

[14] J. Yang, X. Fang, Y. Xu, X. Liu, Investigation of the deactivation behavior of Co catalysts in Fischer–Tropsch synthesis using encapsulated Co nanoparticles with controlled SiO_2 shell layer thickness, Catal. Sci. Technol. 10 (2020) 1182–1192.

[15] L. Li, J. Wu, J. Shao, Z. Tang, Y. Dai, H. Chen, Impacts of SiO_2 shell structure of Ni/SiO_2 nanocatalysts on their performance for catalytic decomposition of ammonia, Catal. Lett. 147 (2017) 141–149.

[16] Y. Xu, G. Ma, J. Bai, Y. Du, C. Qin, M. Ding, Yolk@shell FeMn@hollow HZSM-5 nanoreactor for directly converting syngas to aromatics, ACS Catal. 11 (2021) 4476–4485.

[17] Y. Hu, J. Chen, W. Chen, X. Lin, X. Li, Synthesis of novel nickel sulfide submicrometer hollow spheres, Adv. Mater. 15 (2003) 726–729.

[18] Y. Sheng, H.C. Zeng, Structured assemblages of single-walled 3d transition metal silicate nanotubes as precursors for composition-tailorable catalysts, Chem. Mater. 27 (2015) 658–667.

[19] B. Li, H.C. Zeng, Formation combined with intercalation of Ni and its alloy nanoparticles within mesoporous silica for robust catalytic reactions, ACS Appl. Mater. Interfaces 10 (2018) 29435–29447.

[20] C. Wang, X. Jie, Y. Qiu, Y. Zhao, H.A. Al-Megren, S. Alshihri, P.P. Edwards, T. Xiao, The importance of inner cavity space within $Ni@SiO_2$ nanocapsule catalysts for excellent coking resistance in the high-space-velocity dry reforming of methane, Appl. Catal. B: Environ. 259 (2019), 118019.

[21] Z. Niu, S. Zhang, Y. Sun, S. Gai, F. He, Y. Dai, L. Li, P. Yang, Controllable synthesis of Ni/SiO_2 hollow spheres and their excellent catalytic performance in 4-nitro-phenol reduction, Dalton Trans. 43 (2014) 16911–16918.

[22] Y. Sheng, H.C. Zeng, Monodisperse aluminosilicate spheres with tunable Al/Si ratio and hierarchical macro-meso-microporous structure, ACS Appl. Mater. Interfaces 7 (2015) 13578–13589.

[23] Y. Du, Y. Zhu, S. Xi, P. Yang, H.O. Moser, M.B. Breese, A. Borgna, XAFCA: a new XAFS beamline for catalysis research, J. Synchrotron Radiat. 22 (2015) 839–843.

[24] J. Hu, M. Chen, X. Fang, L. Wu, Fabrication and application of inorganic hollow spheres, Chem. Soc. Rev. 40 (2011) 5472–5491.

[25] H.C. Zeng, Synthesis and self-assembly of complex hollow materials, J. Mater. Chem. 21 (2011) 7511–7526.

[26] D.P. Wang, H.C. Zeng, Creation of interior space, architecture of shell structure, and encapsulation of functional materials for mesoporous SiO_2 spheres, Chem. Mater. 23 (2011) 4886–4899.

[27] Z. Teng, X. Su, Y. Zheng, J. Sun, G. Chen, C. Tian, J. Wang, H. Li, Y. Zhao, G. Lu, Mesoporous silica hollow spheres with ordered radial mesochannels by a spontaneous self-transformation approach, Chem. Mater. 25 (2012) 98–105.

[28] Y. Wang, F. Lin, B. Shang, B. Peng, Z. Deng, Self-template synthesis of nickel silicate and nickel silicate/nickel composite nanotubes and their applications in wastewater treatment, J. Colloid Interface Sci. 522 (2018) 191–199.

[29] Y. Yu, R. Jin, J. Easa, W. Lu, M. Yang, X. Liu, Y. Xing, Z. Shi, Highly active and stable copper catalysts derived from copper silicate double-shell nanofibers with strong metal–support interactions for the RWGS reaction, Chem. Commun. 55 (2019) 4178–4181.

[30] Y. Wu, G. Chang, Y. Zhao, Y. Zhang, Preparation of hollow nickel silicate nanospheres for separation of His-tagged proteins, Dalton Trans. 43 (2014) 779–783.

[31] A.J. Majewski, J. Wood, Tri-reforming of methane over $Ni@SiO_2$ catalyst, Int. J. Hydrog. Energy 39 (2014) 12578–12585.

[32] M. Sivaiah, S. Petit, J. Barrault, C. Batiot-Dupeyrat, S. Valange, CO_2 reforming of CH_4 over Ni-containing phyllosilicates as catalyst precursors, Catal. Today 157 (2010) 397–403.

[33] M. Kosari, A.M. Seayad, S. Xi, S.M. Kozlov, A. Borgna, H.C. Zeng, Synthesis of mesoporous copper aluminosilicate hollow spheres for oxidation reactions, ACS Appl. Mater. Interfaces 12 (2020) 23060–23075.

[34] P. Burattin, M. Che, C. Louis, Characterization of the Ni (II) phase formed on silica upon deposition− precipitation, J. Phys. Chem. B 101 (1997) 7060–7074.

[35] A.J. Majewski, J. Wood, W. Bujalski, Nickel–silica core@ shell catalyst for methane reforming, Int. J. Hydrog. Energy 38 (2013) 14531–14541.

[36] S. Das, J. Ashok, Z. Bian, N. Dewangan, M. Wai, Y. Du, A. Borgna, K. Hidajat, S. Kawi, Silica–Ceria sandwiched Ni core–shell catalyst for low temperature dry reforming of biogas: coke resistance and mechanistic insights, Appl. Catal. B: Environ. 230 (2018) 220–236.

[37] F. Wang, L. Xu, W. Shi, Syngas production from CO_2 reforming with methane over core-shell $Ni@SiO_2$ catalysts, J. CO2 Util. 16 (2016) 318–327.

[38] P. Cao, S. Adegbite, T. Wu, Thermodynamic equilibrium analysis of CO_2 reforming of methane: elimination of carbon deposition and adjustment of H_2/CO ratio, Energy Procedia 105 (2017) 1864–1869.

[39] B. Li, H.C. Zeng, Synthetic chemistry and multifunctionality of an amorphous Ni-MOF-74 shell on a Ni/SiO_2 hollow catalyst for efficient tandem reactions, Chem. Mater. 31 (2019) 5320–5330.

[40] K. Kamonsuangkasem, S. Therdthianwong, A. Therdthianwong, N. Thammajak, Remarkable activity and stability of Ni catalyst supported on CeO_2-Al_2O_3 via $CeAlO_3$ perovskite towards glycerol steam reforming for hydrogen production, Appl. Catal. B: Environ. 218 (2017) 650–663.

[41] L.F. Bobadilla, V. Garcilaso, M.A. Centeno, J.A. Odriozola, Monitoring the reaction mechanism in model biogas reforming by in situ transient and steady-state DRIFTS measurements, ChemSusChem 10 (2017) 1193–1201.

[42] M. Németh, Z. Schay, D. Sranko, J. Károlyi, G. Sáfrán, I. Sajó, A. Horváth, Impregnated Ni/ZrO_2 and Pt/ZrO_2 catalysts in dry reforming of methane: Activity tests in excess methane and mechanistic studies with labeled $^{13}CO_2$, Appl. Catal. A: Gen. 504 (2015) 608–620.

[43] L.F. Bobadilla, V. Garcilaso, M.Á. Centeno, J.A. Odriozola, Monitoring the reaction mechanism in model biogas reforming by in situ transient and steady-state DRIFTS measurements, ChemSusChem 10 (2017) 1193–1201.

[44] E. le Saché, T. Reina, Analysis of dry reforming as direct route for gas phase CO_2 conversion. the past, the present and future of catalytic DRM technologies, Prog. Energy Combust. Sci. 89 (2022), 100970.

[45] B.C. Enger, R. Lødeng, A. Holmen, A review of catalytic partial oxidation of methane to synthesis gas with emphasis on reaction mechanisms over transition metal catalysts, Appl. Catal. A: Gen. 346 (2008) 1–27.

[46] J. Toyir, P. Gélin, H. Belatel, A. Kaddouri, $Ir/Ce_{0.9}Gd_{0.1}O_{2−x}$ as a new potential anode component in solid oxide fuel cells integrating the concept of gradual internal reforming of methane, Catal. Today 157 (2010) 451–455.

[47] M.A. Vasiliades, M. Makri, P. Djinović, B. Erjavec, A. Pintar, A.M. Efstathiou, Dry reforming of methane over 5 wt% $Ni/Ce_{1−x}Pr_xO_{2-δ}$ catalysts: performance and characterisation of active and inactive carbon by transient isotopic techniques, Appl. Catal. B: Environ. 197 (2016) 168–183.

[48] M. Li, A.C. van Veen, Tuning the catalytic performance of Ni-catalysed dry reforming of methane and carbon deposition via $Ni-CeO_{2−x}$ interaction, Appl. Catal. B: Environ. 237 (2018) 641–648.

[49] X. Yan, T. Hu, P. Liu, S. Li, B. Zhao, Q. Zhang, W. Jiao, S. Chen, P. Wang, J. Lu, Highly efficient and stable $Ni/CeO2-SiO_2$ catalyst for dry reforming of methane: effect of interfacial structure of Ni/CeO_2 on SiO_2, Appl. Catal. B: Environ. 246 (2019) 221–231.

[50] J. Zhang, F. Li, Coke-resistant $Ni@SiO_2$ catalyst for dry reforming of methane, Appl. Catal. B: Environ. 176 (2015) 513–521.

[51] Z. Li, Y. Kathiraser, S. Kawi, Facile synthesis of high surface area yolk–shell Ni@Ni embedded SiO_2 via Ni phyllosilicate with enhanced performance for CO_2 reforming of CH_4, ChemCatChem 7 (2015) 160–168.

[52] Z. Bian, S. Kawi, Sandwich-like silica@Ni@silica multicore–shell catalyst for the low-temperature dry reforming of methane: confinement effect against carbon formation, ChemCatChem 10 (2018) 320–328.

[53] T. Xie, L. Shi, J. Zhang, D. Zhang, Immobilizing Ni nanoparticles to mesoporous silica with size and location control via a polyol-assisted route for coking-and sintering-resistant dry reforming of methane, Chem. Commun. 50 (2014) 7250–7253.

[54] S. Zhang, S. Muratsugu, N. Ishiguro, M. Tada, Ceria-doped Ni/SBA-16 catalysts for dry reforming of methane, ACS Catal. 3 (2013) 1855–1864.

[55] J.W. Han, J.S. Park, M.S. Choi, H. Lee, Uncoupling the size and support effects of Ni catalysts for dry reforming of methane, Appl. Catal. B: Environ. 203 (2017) 625–632.

[56] E.C. Lovell, A. Fuller, J. Scott, R. Amal, Enhancing Ni-SiO_2 catalysts for the carbon dioxide reforming of methane: Reduction-oxidation-reduction pre-treatment, Appl. Catal. B: Environ. 199 (2016) 155–165.

[57] F. Wang, B. Han, L. Zhang, L. Xu, H. Yu, W. Shi, CO_2 reforming with methane over small-sized $Ni@SiO_2$ catalysts with unique features of sintering-free and low carbon, Appl. Catal. B: Environ. 235 (2018) 26–35.

[58] S. Wen, M. Liang, J. Zou, S. Wang, X. Zhu, L. Liu, Z.J. Wang, Synthesis of a SiO_2 nanofibre confined Ni catalyst by electrospinning for the CO_2 reforming of methane, J. Mater. Chem. A 3 (2015) 13299–13307.